Development of Cryogenic Bolometer for Neutrinoless Double Beta Decay in ^{124}Sn

By

Vivek Singh

PHYS01200804030

Bhabha Atomic Research Centre, Mumbai – 400 085

A thesis submitted to the

Board of Studies in Physical Sciences

In partial fulfillment of requirements

For the Degree of

DOCTOR OF PHILOSOPHY

of

HOMI BHABHA NATIONAL INSTITUTE

October, 2014

Homi Bhabha National Institute

Recommendations of the Viva Voce Board

As members of the Viva Voce Board, we certify that we have read the dissertation prepared by Vivek Singh entitled "Development of Cryogenic Bolometer for Neutrinoless Double Beta Decay in ^{124}Sn" and recommend that it may be accepted as fulfilling the dissertation requirement for the Degree of Doctor of philosophy.

Chairman - Prof. S. L. Chaplot	**Date:**
Guide / Convener - Prof. V. Nanal	**Date:**
Co-guide - Prof. V. M. Datar	**Date:**
Member - Dr. G. Ravikumar	**Date:**
Member - Prof. R. G. Pillay	**Date:**
Member - Dr. V. Ganesan	**Date:**

Final approval and acceptance of this dissertation is contingent upon the candidate's submission of the final copies of the dissertation to HBNI.

I/We hereby certify that I/we have read this dissertation prepared under my/our direction and recommend that it may be accepted as fulfilling the dissertation requirement.

Date:

Place:

Co-guide **Guide**

STATEMENT BY AUTHOR

This dissertation has been submitted in partial fulfillment of requirements for an advanced degree at Homi Bhabha National Institute (HBNI) and is deposited in the Library to be made available to borrowers under rules of the HBNI.

Brief quotations from this dissertation are allowable without special permission, provided that accurate acknowledgement of source is made. Requests for permission for extended quotation from or reproduction of this manuscript in whole or in part may be granted by the Competent Authority of HBNI when in his or her judgement the proposed use of the material is in the interests of scholarship. In all other instances, however, permission must be obtained from the author.

Vivek Singh

DECLARATION

I, hereby declare that the investigation presented in the thesis has been carried out by me. The work is original and has not been submitted earlier as a whole or in part for a degree / diploma at this or any other Institution / University.

Vivek Singh

List of Publications arising from the thesis

Journal

1. "Heat capacity setup for superconducting bolometer absorbers below 400mK", **V. Singh**, Mathimalar. S, N. Dokania, V. Nanal, R. G. Pillay, S. Ramakrishnan, *Journal of Low temperature Physics*, **2014**, *175*, 604-613.
2. "Cryogen Free Dilution Refrigerator for bolometric search of neutrinoless double decay ($0\nu\beta\beta$) in ^{124}Sn", **V. Singh**, Mathimalar. S, N. Dokania, V. Nanal, R. G. Pillay, S. Ramakrishnan, *Pramana - Journal of Physics*, **2013**, *81*, 719-725.
3. "Simulation studies for the Tin Bolometer Array for Neutrinoless Double Beta Decay", **V. Singh**, Mathimalar. S, N. Dokania, V. Nanal, R. G. Pillay, *Pramana - Journal of Physics* (*submitted*)

Conferences

1. "Development of Cryogenic Bolometer for $0\nu\beta\beta$ in ^{124}Sn", **V. Singh**, G. Yashwant, S. Mathimalar, Neha Dokania, V. Nanal, R. G. Pillay, V. M. Datar, *AIP Conf. Proc.*, **2011**, *1405*, 334-336.
2. "Simulation study of Sn bolometer for NDBD", **V. Singh**, Y. Gowda, V. Nanal, R.G. Pillay, *Proceedings of the Int. Symp. on Nucl. Phys.*, **2009**, *54*, 614-615.

Others

1. "Study of neutron-induced background and its effect on the search of ($0\nu\beta\beta$) in decay of ^{124}Sn", N. Dokania, **V. Singh**, S. Mathimalar, C. Ghosh, V. Nanal, R.G. Pillay, S. Pal, K.G. Bhushan, A. Shrivastava, *Journal of Instrumentation* (*accepted*).
2. "Characterization and modeling of a low background HPGe detector", N. Dokania,**V. Singh**, S. Mathimalar, V. Nanal, S. Pal, R. G. Pillay, *Nuclear Instruments and Methods in Physics Research A*, **2014**, *745*, 119-127.
3. "Testing of the PARIS $LaBr_3$-NaI Phoswich Detector with High Energy Gamma-rays", M. Zieblinski , M. Jastrzab , Neha Dokania, V. Nanal, S. Brambilla, P. Bednarczyk, M. Ciemala, E. Dutkiewicz, M. Kmiecik, M. Krzysiek, J. Lekki, A. Maj, Z. Szklarz, B. Wasilewska, M. Dudelo, K. Hadynska-Klek, P. Napiorkowski, B. Genolini, Ch. Schmitt, W. Catford, M. Nakhostin, N. Yavuzkanat, O. Dorvaux, R.G.

Pillay, M.S. Pose, S. Mishra, S. Mathimalar, **V. Singh**, N. Katyan, D.R. Chakrabarty, V.M. Datar, Suresh Kumar, G. Mishra, S. Mukhopadhyay, D. Pandit, S. Erturk, *Acta Phys. Pol. B*, **2013**, *44*, 651.

4. "Measurement of the Damping of the Nuclear Shell Effect in the Doubly Magic ^{208}Pb Region", P. C. Rout, D. R. Chakrabarty, V. M. Datar, Suresh Kumar, E. T. Mirgule, A. Mitra, V. Nanal, S. P. Behera and **V. Singh**, *Phys. Rev. Lett.*, **2013**, *110*, 062501.

5. "Fusion and quasi-elastic scattering in ^{6,7}Li + ^{197}Au systems", C.S. Palshetkar, Shital Thakur, V. Nanal, A. Shrivastava, N. Dokania, **V. Singh**, V.V. Parkar, P.C. Rout, R. Palit, R.G. Pillay, S. Bhattacharyya, A. Chatterjee, S. Santra, K. Ramachandran, and N.L. Singh, *Phys. Rev. C*, **2014**, *89*, 024607

6. "Study of radioactive impurities in neutron transmutation doped Ge", S. Mathimalar, N. Dokania, **V. Singh**, V. Nanal, R.G. Pillay, A. Shrivastava, K.C. Jagadeesan, S.V. Thakare, *Nucl. Instr. and Meth. A.* (*submitted*)

7. "Characterization of neutron transmutation doped (NTD) Ge for low temperature sensor development", S. Mathimalar,**V. Singh**, N. Dokania, V. Nanal, R. G. Pillay, S. Pal, S. Ramakrishnan, A. Shrivastava, Priya Maheswari, P. K. Pujari, S. Ojha, D. Kanjilal, K.C. Jagadeesan and S.V. Thakare, *Nucl. Instr. and Meth. B* (*submitted*).

8. "Specific Heat of Teflon, Torlon - 4203 and Torlon - 4301 in the range of 30 - 400 mK", **V. Singh**, A. Garai, Mathimalar. S, N. Dokania, V. Nanal, R. G. Pillay, S. Ramakrishnan, *Cryogenics - Journal* (*submitted)*

Vivek Singh

Dedicated to

My Parents & My Sister

and the tax payers of the country who fund scientific research.

ACKNOWLEDGMENTS

The research included in this dissertation could not have been performed if not for the assistance, patience and support of many individuals. I would like to express my deepest gratitude to my advisor Prof. Vandana Nanal, not only for her scientific guidance and valuable advice during my graduate study but also for giving me the freedom to develop my own ideas independently. I am also greatly indebted to Prof. R.G. Pillay for his supervision, brilliant insights, helpful comments and suggestions which have improved my understanding of the subject. I thank Dr. Y. Gowda, Mathimalar and Neha for the fruitful collaboration and all the discussions we have had, scientific or not, during the last five years. For work covered in this thesis, I gratefully acknowledge the enlightening interactions with Prof. S. Ramakrishnan and Prof. Vivek Datar. I am also grateful to Prof. V. Tretyak for several helpful correspondences. I thank, Prof. Naba Mondal, Prof. S.N. Mishra and Prof. R. Palit for keeping a keen interest in my progress. My sincerest thanks are due to LINAC and Central Workshop staff members and would like to extend my gratitude to Mr. M.S. Pose, Mr. J.N. Karande, Mr. S.M. Powale, Mr. A.A. Shinde and Mr. K.S. Divekar. I thank my friends and colleagues Amaresh, Anushree, Chandan, Deepak, Devika, Gourab, Jasmine, Nilay, Nitali, Parul, Sadhana, Saurav, Shital, Sudeshna, Sudipta and Sumanta for making my stay at TIFR a memorable experience. Last but not the least, I thank my family for their unconditional love and unwavering support.

TABLE OF CONTENTS

LIST OF FIGURES

Figure **Page**

LIST OF TABLES

SYNOPSIS

The observation of neutrino oscillations [1–5], which implies finite neutrino mass, is one of the most important discoveries in particle physics in recent years. However, the absolute mass of neutrinos and its true nature are not known yet. Neutrinos can either be Dirac (with particles and antiparticles being distinct) or Majorana (with particles and antiparticles being indistinguishable) particles. Understanding the nature of neutrinos is of fundamental importance to explain the origin of small neutrino masses and possibly to elucidate the matter-antimatter asymmetry observed in nature [6].

Double beta decay ($\beta\beta$) is a second order process involving the weak interaction in which an initial nucleus (A, Z) decays to its isobar (A, Z+2) with the emission of two electrons. In some nuclei [7], the decay of an even-even parent nuclei (A, Z) to the neighboring odd-odd nuclei (A, Z+1) is energetically and/or spin forbidden (or strongly suppressed) and the double beta decay to (A, Z+1) is the only available decay channel. This is due to the pairing force in the nucleus which renders the even–even nuclei with an even number of protons and neutrons more stable than the odd–odd nuclei with

an unpaired proton and neutron. Two neutrino double beta decay ($2\nu\beta\beta$), which involves emission of two electrons and two antineutrinos, is fully consistent with Glashow-Weinberg-Salam model of electroweak theory [8–10] and has been observed experimentally in few isotopes [11]. However, if neutrinos are Majorana particles then the nuclei can undergo neutrinoless mode of $\beta\beta$ decay, where the final state has only two electrons and no antineutrinos are emitted. This process violates lepton number conservation and is forbidden in the standard model of electroweak interaction. Moreover, observation of $0\nu\beta\beta$ would necessarily imply the existence of a Majorana mass term for the neutrino for any standard model like gauge theory [12]. Hence, neutrinoless double beta decay ($0\nu\beta\beta$) is the golden channel to probe the true nature of neutrinos. The experimental signature for $0\nu\beta\beta$ is a mono–energetic peak in the electron sum energy spectrum corresponding to the Q value of the decay. In addition, the $0\nu\beta\beta$ experiments measure the rate of transition of $0\nu\beta\beta$ decay, which is given by [13, 14]

$$(T^{0\nu}_{1/2})^{-1} = G_{0\nu}(Q_{\beta\beta}, Z)|M_{0\nu}|^2 < m_{\beta\beta} >^2 \qquad (1)$$

where $G_{0\nu}(Q_{\beta\beta}, Z)$ is the phase-space factor for the emission of the two electrons, $M_{0\nu}$ is the nuclear matrix element and $< m_{\beta\beta} >$ is the effective Majorana mass of the electron neutrino. Given its importance, several experiments around the world are investigating the $0\nu\beta\beta$ process employing

different detection techniques [15]. Currently the results from calculations of nuclear matrix elements are model dependent [16] and introduce a significant uncertainty in the extraction of the effective neutrino mass. Therefore, it is extremely important to measure the $0\nu\beta\beta$ transition rates in different nuclei.

A feasibility study to setup an experiment to search for $0\nu\beta\beta$ in ^{124}Sn at the upcoming underground facility, the India based Neutrino Observatory (INO) has been initiated [17]. One of the experimental approaches to observe the $0\nu\beta\beta$ decay signal is based on cryogenic particle detectors. Cryogenic calorimetric particle detectors (bolometers), where the energy of impinging radiation is converted into phonons leading to a measurable temperature rise, have excellent energy resolution and high sensitivity [18]. Bolometers when operated at temperature below 50 mK have extremely small heat capacity and are sensitive to even small amounts of energy released in a large absorber. Pure insulators as well as superconductors, are good candidates for bolometers as their specific heat falls off rapidly at these low temperatures. The isotope ^{124}Sn is a good candidate for search of $0\nu\beta\beta$ as it has reasonably high Q value (2292.6 ± 0.39 keV [19]), moderate isotopic abundance (5.8%) and can be made into a cryogenic bolometer with high energy resolution [20, 21]. Tin becomes superconducting at 3.17 K and at temperatures below 100 mK the specific heat has only the phononic

contribution. Thus, a tin bolometer operating at $\sim$10 mK temperature is an ideal choice for a high energy resolution detector. It is envisaged that the prototype of Tin.Tin (The India based Tin detector) would consist of an array of $\sim$ 30 Tin detector elements (natural/enriched $\sim$ 3 x 3 x 3 cm^3 each) arranged in a tower geometry with corresponding readout sensors. Continuous cooling of these bolometers below 1K will be achieved using a dilution refrigerator [22, 23].

This thesis work is mainly focused on R&D related to the fabrication of a large size Sn (superconducting) cryogenic bolometer. The design, installation and optimization of the cryogenic system necessary for prototype development has been performed. Simulation and test studies for the 3 x 3 x 3 cm^3 prototype detector element have also been performed. Both the aspects are described briefly in the following paragraphs.

Cryogen Free Dilution Refrigerator (CFDR-1200):

A custom built cryogen free dilution refrigerator, CFDR-1200, with a high cooling power of 1.4 mW at 120 mK, has been successfully installed and tested at TIFR, Mumbai [24]. Given the long time scale of $0\nu\beta\beta$ experiment and the remote location of an underground laboratory, the choice of a cryogen free dilution refrigerator instead of the conventional wet system (which requires liquid helium supply), is imperative. Since the sensitivity of

the $0\nu\beta\beta$ experiment is crucially dependent on the minimization of background radioactivity, it is essential that the material surrounding the detector elements should be of high radio-purity. In addition, a bulk shielding is highly desirable inside the cryostat to suppress the background events arising from the materials used for cryostat construction. Therefore, a provision for additional low activity shielding inside the cryostat is also incorporated in the design. The dilution refrigerator has a cylindrical sample space of 300 mm x 300 mm available below the Mixing Chamber (MC) which is inside the inner most 50 mK shield and can support a total mass of $\sim$ 100 kgs (Sn detector and $\sim$ 5cm thick low activity lead shield). The CFDR-1200 is equipped with readout wiring for up to 75 sensors (4 probe measurement). The minimum base temperature of $<$10 mK has been measured using a calibrated Cerium Magnesium Nitrate (CMN) thermometer and a carbon Speer resistor. After optimizing the operating conditions (flow rate), the performance of CFDR-1200 has been found to be consistent with the Takano's model [25] for conventional refrigerators. The higher flow rate has resulted in a greater cooling power with a significantly smaller quantity of ^{3}He as compared to a standard wet dilution refrigerator.

Design of prototype detector module:

The performance of bolometers as thermal radiation detectors is determined

by their efficiency to measure the change in temperature against the thermodynamic energy fluctuation present in the system. The heat capacity of the absorbing material is the most crucial aspect in a calorimetric particle detector construction as the intrinsic resolution of a calorimeter is strongly dependent on its heat capacity [26]. Although tin micro-calorimeters have shown excellent energy resolution, large size tin bolometers have not yet been made. It is reported that the spectral resolution of superconducting bolometers is limited by the incomplete thermalization of energy in the absorber materials and has been attributed to energy trapping by quasiparticles with long lifetime in superconductors [27, 28]. It is also quite well known that a small amount of impurity can give rise to high specific heat at these low temperatures. Hence, the heat capacity of these samples at low temperature has been investigated to check if anomalous specific heat affects the energy resolution. A calorimeter set up has been devised to measure the extremely small heat capacity of superconductors below 400 mK using Carbon sensors made from commercially available Carbon resistors. The setup is inexpensive and uses off-the-shelf low temperature electronics to measure the heat capacity. The specific heat of Tin has been measured on the setup in the range of 60-400 mK and has been found to be in good agreement with the earlier reported values of Tin which corresponds to a Debye temperature of Θ_D = 200 K. The absence of anomalous heat capacity in the Tin sample

at ultra low temperature along with the result of quasiparticle lifetime saturation by Visser *et.al*. [29] suggests that it should be possible to achieve complete thermalization of energy in a Tin bolometer absorber. Moreover, size of detector element has been optimized for a measurable temperature rise and reduced granularity to minimize number of readout channels. The latter point is also important as increased number of sensors correspond to larger surrounding material (connecting wires etc.) which can contribute to the background. Using Monte-Carlo simulation, based on the GEANT4 package, the possibility to use hit multiplicity (M) for discrimination between electrons ($M = 1$) and gamma rays ($M \geq 1$) has been demonstrated. Further, the ($0\nu\beta\beta$) events are simulated inside the detector and an efficiency factor for the optimized crystal size has been obtained.

In the first chapter of the thesis, neutrinoless double beta decay is introduced along with brief description of the theory of neutrino oscillation and neutrino masses. A review of current ($0\nu\beta\beta$) experiments is presented. The chapter also includes an introduction to the bolometric technique with focus on Sn macro-bolometers for the search of $0\nu\beta\beta$ decay.

Chapter 2 describes the design and performance optimization of CFDR-1200 dilution refrigerator. The principle of operation of the dilution refrigerator will be introduced. Results obtained during installation tests and operational parameters of CFDR-1200 are presented.

The third chapter gives a brief description of heat capacity measurement techniques at ultra-low temperature. Development of the setup and the procedure to measure the heat capacity of superconducting calorimeter absorbers below 100 mK along with results for Sn are presented.

The Monte-Carlo simulation of $0\nu\beta\beta$ events in the detector and the optimization of the size of a detector element is presented in the fourth chapter. This chapter also describes simulation results pertinent to $e^- - \gamma$ discrimination in bolometers employing hit multiplicity.

Chapter 5 contains the summary. The future outlook for a large scale design of TIN.TIN is described.

BIBLIOGRAPHY

[1] Super-Kamiokande, R.Wendell et al., Phys. Rev. D **81** (2010) 092004

[2] SNO, B. Aharmim et al., Phys.Rev. C **88** (2013) 025501

[3] KamLAND, A. Gando et al., Phys. Rev. D **83** (2011) 052002

[4] K2K, M.H. Ahn et al., Phys. Rev. Lett. **90** (2003) 041801

[5] MINOS, P. Adamson et al., Phys. Rev. Lett. **106** (2011) 181801

[6] M. Fukugita, T. Yanagida, Phys. Lett. B **174** (1986) 45

[7] V. I. Tretyak, Y. G. Zdesenko, Atomic Data and Nuclear Data Tables **80** (2002) 83

[8] S.L. Glashow, Nucl. Phys. **22** (1961) 579

[9] S. Weinberg, Phys. Rev. Lett. **19** (1967) 1264

[10] A. Salam, N. Svartholm (Ed.), Proc. 8-th Nobel Symp., Almquist and Wiksell, Stockholm (1968) 367

[11] A. S. Barabash, Physics of Atomic Nuclei **74** (2011) 603

[12] J. Schechter and J. W. F. Valle, Phys. Rev. D **25** (1982) 2951

[13] F.T. Avignone III, S.R. Elliott and J. Engel, Rev. Mod. Phys. **80** (2008) 481

[14] K. Zuber, Pramana -Journal of Physics **79** (2012) 781-791

[15] A. S. Barabash, Physics of Particles and Nuclei **42** (2011) 613

[16] F. Simkovic, Physics of Particles and Nuclei Letters **10** (2013) 623

[17] V. Nanal, EPJ Web of Conferences **66** (2014) 08005

[18] G.C. Hilton, AIP Conf. Proc. **1185** (2009) 3

[19] D.A. Nesterenko et. al. Phys. Rev. C **86** (2012) 044313

[20] M. K. Bacrania et. al., IEEE Trans. Appl. Supercond. **56** (2009) 2299

[21] D.A. Bennett et. al., Rev. Sci. Instrum. **83** (2012) 093113

[22] O.V. Lounasmaa, Experimental Principles and Methods Below 1 K, (Academic, London 1974)

[23] F. Pobell, Matter and Methods at Low Temperatures, 3rd Edition (Springer, 2007)

[24] V. Singh, Mathimalar. S, N. Dokania, V. Nanal, R.G. Pillay, S. Ramakrishnan, Pramana - Journal of Physics **81** (2013) 719

[25] Y. Takano, Rev. Sci. Instrum. **65** (1994) 1667

[26] C. Enss and D. McCammon, J. Low Temp Phys. **151** (2008) 5

[27] E. Cosulich *et. al.*, Journal Low Temp. Phys. **93** (1993) 263

[28] E. Perinati, M. Barbara, A. Collura, S. Serio, E. Silver, Nucl. Instrum. Meth. A **531** (2004) 459

[29] P. J. de Visser *et. al.*, Physical Review Letters **106** (2011) 167004

Chapter 1

Introduction

Neutrinos were first theoretically postulated in 1930 by W. Pauli to reconcile data on nuclear beta decay with conservation of energy-momentum and angular momentum. The observed continuous energy spectrum of electrons emitted in β decay was explained by introducing a new spin $\frac{1}{2}$ particle (now called neutrino). The postulated neutrino was a massless or a very light neutral particle that was produced together with the electron, sharing the transition energy, but escaping detection. The understanding of β decay changed rapidly after the discovery of the neutron and was successfully explained by Fermi's theory of β–decay [1]. Shortly afterwards M. Goeppert-Mayer, in 1935, identifed the possibilty of a nucleus (A, Z) tranforming to its (A, Z+2) isobar by simultenous emission of two electrons and two neutrinos [2].

$$(A,Z) \rightarrow (A,Z+2) + 2e^{-} + 2\overline{\nu_e} \tag{1.1}$$

Its measurement would only be possible in cases where single beta decay of a nucleus is forbidden/strongly suppressed due to energy and spin. In 1937 Majorana published his work on "Symmetrical theory of the electron and positron" [3]. At that time the existing theory of electrons and positrons treated positrons as holes in the Dirac sea of states of electrons with negative energy. Majorana symmetrized the electron-positron theory in which there were no states with negative energies and realized that symmetry properties of Dirac's theory allowed the possibility for electrically neutral spin $\frac{1}{2}$ fermions to be their own antiparticles.

Soon afterwards Racah suggested the following chain reaction in a nucleus to test whether neutrino is a Majorana or Dirac particle.

$$(A,Z) \rightarrow (A,Z+1) + e^- + \nu, \tag{1.2}$$

$$\nu + (A',Z') \rightarrow (A',Z'+1) + e^- \tag{1.3}$$

In 1939 Wendell Furry for the first time considered neutrinoless double beta decay ($0\nu\beta\beta$) of nuclei,

$$(A,Z) \rightarrow (A,Z+2) + 2e^- \tag{1.4}$$

which is essentially a Racah chain of reaction with virtual neutrinos [4]. At that time it was believed that the decay rate of $0\nu\beta\beta$ was much more favorable than the $2\nu\beta\beta$ decay due to the former's increased phase space. The phase space for $0\nu\beta\beta$ decay is about 10^6 times larger than that for $2\nu\beta\beta$ decay corresponding to a larger number of final states available. This is due to the fact the virtual neutrino in Eqn. 1.4 is constrained inside the volume of the nuclei which, according to Heisenberg's uncertainty principle, requires states up to 100 MeV to be taken into account. However, in $2\nu\beta\beta$ decay, where real neutrinos are emitted, the number of final states is limited by the Q value (< 5 MeV) of the decay.

The understanding of decay rates changed drastically in 1957 when maximal parity violation in beta decay was discovered by Wu *et.al.* [5]. Primakoff and Rosen in their seminal work recognized that due to chirality suppression the relative rate of $0\nu\beta\beta$ is much smaller ($\sim 10^6$) than the decay rate of $2\nu\beta\beta$ [6]. Given the rarity of the process, experiments with large targets, extremely low background and high energy resolution have to be designed to probe the Majorana nature of the neutrino. Neutrino masses require either the existence of right-handed neutrinos or violation of the lepton number so that Majorana masses are possible. It has been proved by Schechter and Valle that observation of $0\nu\beta\beta$ would necessarily imply the existence of a Majorana mass term for the neutrino for any standard model

like Gauge theory [7]. Hence, $0\nu\beta\beta$ decay is the golden channel to probe the true nature of neutrinos.

1.1 Dirac and Majorana neutrinos

The Dirac equation 1.5, which is Lorentz covariant, describes all the spin $\frac{1}{2}$ particles.

$$(i\gamma^{\mu}\partial_{\mu} - m)\psi = 0 \tag{1.5}$$

The gamma matrices satisfies the anti-commutation rule $\{\gamma^{\mu}, \gamma^{\nu}\} = 2\eta^{\mu\nu}$ where $\eta^{\mu\nu}$ is the Minkowski metric on space-time. Eqn. 1.5 can be derived from the Lagrangian density for a Dirac field given by

$$\mathscr{L} = i\overline{\psi}\gamma^{\mu}\partial_{\mu}\psi - m\overline{\psi}\psi \tag{1.6}$$

where $\overline{\psi} = \psi^{\dagger}\gamma^{0}$. It is easily seen from Eqns. 1.5 and 1.6 that a term of the form $\overline{\psi}\psi$ in the Lagrangian is responsible for giving mass to a spin $\frac{1}{2}$ particle. The solution to Eqn. 1.5 is a 4 component bi-spinor vector

$$\psi = (\psi_1, \psi_2, \psi_3, \psi_4)^T \tag{1.7}$$

which can be further recast into

$$\psi \equiv \begin{pmatrix} \psi_L \\ \psi_R \end{pmatrix}. \tag{1.8}$$

ψ_L and ψ_R are the left-handed and right-handed projections of the spinor ψ. A particle is defined as left-handed (right-handed) if the spin of the particle is in the same (opposite) direction as its momentum.

$$\psi_L = P_L\psi = \frac{1}{2}(1-\gamma^5)\psi \; ; \; \psi_R = P_R\psi = \frac{1}{2}(1+\gamma^5)\psi. \tag{1.9}$$

where the projection operators P_L and P_R satisfy the relations

$$P_L\, P_R = P_R\, P_L = \; 0 \text{ and } P_L \; + \; P_R = \mathbb{I}. \tag{1.10}$$

Using Eqns. 1.9 and 1.10, the mass term of Eqn. 1.6 becomes

$$\mathscr{L}_D = -m_D \, (\overline{\psi_R} \; \psi_L \; + \; \overline{\psi_L} \; \psi_R) \tag{1.11}$$

If Eqn. 1.11 is the origin of neutrino masses, then right-handed chiral neutrinos must exist. The fact that presently there is no experimental evidence for right-handed neutrinos and that the neutrinos masses are very small compared to other leptons and quarks, indicate that there must be other mechanisms which could explain neutrino masses.

If the $\gamma's$ in the Dirac equation are all are purely imaginary then the Eqn. 1.5 will have real solutions. This results in the Majorana condition that ψ and its CP partner are identical i.e., Majorana particles are their own antiparticles. A Majorana field which is Lorentz covariant can be written as

$$\psi^{C}_{L(R)} = i\gamma^2\gamma^0\overline{\psi}^{T}_{L(R)} \tag{1.12}$$

where the operator CP is given by $i\gamma^2\gamma^0$. The Majorana mass term can then be written as

$$\mathscr{L}_M = -M\,(\overline{\psi^{C}_{R}}\;\psi_R\;+\;\overline{\psi_R}\;\psi^{C}_{R}) \tag{1.13}$$

which is formed from right-handed neutrino fields and left-handed antineutrino fields. A charged particle cannot have Majorana mass as the Majorana mass term in the Lagrangian provides a direct coupling between a particle - antiparticle and hence would violate the law of charge conservation. Since neutrinos are neutral spin $\frac{1}{2}$ particles there is a possibility that they are their own antiparticles, in which case they would be referred to as Majorana neutrinos.

1.2 Neutrino Masses and Mixing

In 1956 the first direct observation of the electron antineutrino from a nuclear reactor was performed by a group led by C. Cowan and F. Reines [8].

Subsequently, measurements of neutrinos produced in the sun, atmosphere, reactors and accelerators indicate that the neutrinos oscillate from one 'flavor' to another as a consequence of non-zero mass of neutrinos [9]. Neutrinos (antineutrinos) which take part in the standard charged current (CC) and neutral current (NC) weak interaction are of three types or flavors: $\nu_e(\overline{\nu_e})$, $\nu_\mu(\overline{\nu_\mu})$ and $\nu_\tau(\overline{\nu_\tau})$. Neutrinos (antineutrinos) are always produced in weak interaction processes in a state which is predominantly left-handed (LH) (right-handed (RH)). In the Standard Model (SM) of particle physics the LH charged leptons ($l = e, \mu, \tau$) and LH neutrinos (ν_{lL}) form a weak isospin doublet under $SU(2)_L$ gauge symmetry and couple to the massive $W^\pm$ and Z^0 gauge bosons. The interaction of neutrinos in the SM is described by

$$\mathscr{L} = \sum_{l=e,\mu,\tau} (\underbrace{-\frac{g}{\sqrt{2}}\overline{\nu}_{lL}\gamma^\alpha l_L W^+_\alpha - \frac{g}{\sqrt{2}}\overline{l_L}\gamma^\alpha \nu_{lL} W^-_\alpha}_{\text{CC}} \underbrace{-\frac{g}{2Cos\theta_W}\overline{\nu}_{lL}\gamma^\alpha \nu_{lL} Z_\alpha}_{\text{NC}}) \tag{1.14}$$

where g is the $SU(2)$ gauge coupling constant and θ_W the weak mixing angle. There has been no evidence of RH neutrinos ν_{lR} and they are treated $SU(2)_L$ singlet states. These singlet neutrino states do not couple to the weak gauge bosons and hence their interaction with matter should be much weaker than the weak interaction even if they exist. If right-handed neutrinos exist, they could explain several phenomena which require physics

beyond the SM, including the origin of neutrino masses, neutrino oscillations, and the baryon asymmetry of the universe.

The three flavor eigenstates $\nu_l(l = e, \mu, \tau)$ of the weak interaction are different from the mass eigenstates $\nu_i(i = 1, 2, 3)$ which are responsible for propagation of neutrinos. Either set of eigenstates form an independent orthonormal basis in Hilbert space and hence can be transformed into each other. An important consequence of this would be the possibility of neutrino oscillations as first predicted by Bruno Pontecorvo in 1957 [10, 11]. The possibility of arbitrary mixing between two massive neutrino states was first introduced by Z. Maki, M. Nakagawa and S. Sakata in 1962 [12].

The weak eigenstates $\nu_l(l = e, \mu, \tau)$ are, in general, linear combinations of mass eigenstates $\nu_i(i = 1, 2, 3)$

$$|\nu_l\rangle = \sum_{i=1}^{3} U_{li} |\nu_i\rangle \tag{1.15}$$

In the case of 3 neutrinos, the neutrino mixing matrix U (referred as PMNS matrix, named after Pontecorvo, Maki, Nakagawa and Sakata) can be parametrized by 3 angles and 1 or 3 CP violation (CPV) phases, depending on whether the massive neutrinos are Dirac or Majorana particles,

$$U = R_{23}(\theta_{23})\Phi(\delta)R_{13}(\theta_{13})\Phi^{\dagger}(\delta)R_{12}(\theta_{12}).diag(1, e^{\frac{i\alpha_{21}}{2}}, e^{\frac{i\alpha_{31}}{2}}) \tag{1.16}$$

where $\Phi(\delta) \equiv diag.(1,1,e^{i\delta})$ and θ_{ij} are neutrino mixing angles. δ is the CP violating phase which is non-zero if the neutrino oscillations violate CP–symmetry. The other phases α_{21} and α_{31} are non zero only if the neutrinos are Majorana particles and does not have any effect on neutrino oscillation. The matrices R_{ij} are given by

$$R_{23} = \begin{pmatrix} 1 & 0 & 0 \\ 0 & c_{23} & s_{23} \\ 0 & -s_{23} & c_{23} \end{pmatrix} R_{13} = \begin{pmatrix} c_{13} & 0 & s_{13} \\ 0 & 1 & 0 \\ -s_{13} & 0 & c_{13} \end{pmatrix} R_{12} = \begin{pmatrix} c_{12} & s_{12} & 0 \\ -s_{12} & c_12 & 0 \\ 0 & 0 & 1 \end{pmatrix} \tag{1.17}$$

where c_{ij} and s_{ij} denote $cos(\theta_{ij})$ and $sin(\theta_{ij})$, respectively. Using Eqn. 1.15 and assuming that the neutrinos are ultrarelativistic the probability that a neutrino flavor eigenstate ν_l after a flight distance L and of energy E will be converted to another flavor eigenstate $\nu_{l'}$ can be calculated as [13, 14]

$$P_{ll'} = \delta_{ll'} - 4\sum_{i>j} \text{Re}\,(U^*_{li}U_{l'i}U_{lj}U^*_{l'j}) sin^2\left(\frac{\Delta m^2_{ij}\,L}{4E}\right) + 2\sum_{i>j} \text{Im}\,(U^*_{li}U_{l'i}U_{lj}U^*_{l'j}) cos\left(\frac{\Delta m^2_{ij}\,L}{2E}\right) \tag{1.18}$$

The last term vanishes if there is no CP term. An experiment is sensitive to a given value of Δm^2_{ij} if $E/L \sim \Delta m^2_{ij}$. If $E/L << \Delta m^2_{ij}$ then the oscillating phase undergoes many cycles and the phase will be averaged out ($< sin^2\theta >_{avg.}$ = 1/2). On the contrary, if $E/L >> \Delta m^2_{ij}$ then the phase

inside the sine term will be very small implying that the condition won't be sufficient to give an appreciable oscillation effect.

Table 1.1: Sensitivity of Δm^2 to baseline L and various neutrino sources [9]

Source	Neutrino type	E (MeV)	L (km)	min (Δm^2) (eV^2)
Reactor	$\overline{\nu}_e$	~ 1	1	$\sim 10^{-3}$
Reactor	$\overline{\nu}_e$	~ 1	100	$\sim 10^{-5}$
Accelerator	$\nu_\mu, \overline{\nu}_\mu$	$\sim 10^3$	1	~ 1
Accelerator	$\nu_\mu, \overline{\nu}_\mu$	$\sim 10^3$	1000	$\sim 10^{-3}$
Atmospheric ν's	$\nu_{\mu,e}, \overline{\nu}_{\mu,e}$	$\sim 10^3$	10^4	$\sim 10^{-4}$
Sun	ν_e	~ 1	$1.5\text{x}10^8$	$\sim 10^{11}$

Table 1.1 gives the sensitivity of different oscillation experiments with characteristic values of L and E for various neutrino sources and experiments. The existence of neutrino oscillations gives compelling evidence that the neutrinos have mass, although very small. Many parameters of the PMNS matrix have been determined. In particular, two mass square differences ($\Delta m^2_{sol} \equiv \Delta m^2_{21}$ and $\Delta m^2_{atm} \equiv \Delta m^2_{32}$) have been measured to better than 5% (see Table 1.2). The three neutrino oscillation parameters has been determined from the recent results of the SNO [15], Super Kamiokande [16], KamLAND [17], MINOS [18], K2K [19], Daya Bay [20], RENO [21] and Double Chooz experiments [22]. The following are still unknown:

- **Mass hierarchy of neutrinos**: The oscillations experiments measure only mass squared differences and the mixing parameters, and hence

cannot give information about the absolute neutrino mass. The oscillation data and our understanding of the depleted solar neutrino flux in terms of the MSW matter effect is compatible with two types of non–equivalent neutrino mass spectrum (see Figure 1.1), namely

1. Normal hierarchy: $m_1 < m_2 < m_3$ with $\Delta m^2_{sol} = m^2_2 - m^2_1$ and $\Delta m^2_{atm} = m^2_3 - m^2_1 \simeq m^2_3 - m^2_2$.
2. Inverted hierarchy: $m_3 < m_1 < m_2$ with $\Delta m^2_{sol} = m^2_2 - m^2_1$ and $\Delta m^2_{atm} = m^2_1 - m^2_3 \simeq m^2_2 - m^2_3 \gg \Delta m^2_{sol}$.

- **The absolute mass scale of neutrinos**: The mass of the lightest neutrino is unknown and depending on its value the neutrino mass can also be

  1. Normal: $m_1 < m_2 \ll m_3$ with $m_2 \simeq (\Delta m^2_{sol})^{\frac{1}{2}}$ and $m_3 \simeq \mid \Delta m^2_{atm} \mid^{\frac{1}{2}}$.
  2. Inverted : $m_3 \ll m_1 < m_2$ with $m_{1,2} \simeq \mid \Delta m^2_{atm} \mid^{\frac{1}{2}}$.
  3. Quasi-degenerate $m_1 \simeq m_2 \simeq m_3$ with $m_j \gg \mid \Delta m^2_{atm} \mid^{\frac{1}{2}}$.

- **The CP – violating phases**: The global fits to the neutrino data suggests that $\delta \sim \pi$ but the experimental evidence is not conclusive. The Majorana phases α_{21} and α_{31} are unphysical if neutrinos are not Majorana particles. They cannot be probed by oscillation experiments as they can be absorbed into redefinitions of the fields.

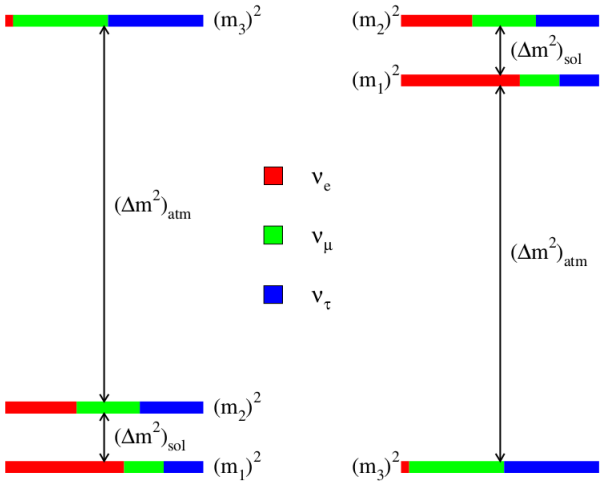

Figure 1.1: Normal (left) and inverted (right) hierarchy for the neutrino mass spectrum. The red, green and blue colours represent ν_e, ν_μ and ν_τ components in the respective mass eigenstates.

Table 1.2 shows the best fit values of the 3–neutrino oscillation parameters after a global analyses of the oscillation data [23, 24]. Neutrinoless

Table 1.2: Best fit data of the three oscillation parameters derived from the global fit [23]. The values for $\Delta m^2 = m_3^2 - (m_2^2 + m_1^2)/2$ correspond to normal (inverted) hierarchy.

Parameters	best–fit ($\pm 1\sigma$)
$\Delta m^2_{21}[10^{-5} eV^2]$	$7.54^{+0.26}_{-0.22}$
$\Delta m^2[10^{-3} eV^2]$	$2.43^{+0.06}_{-0.10}(2.42^{+0.07}_{-0.11})$
$sin^2\theta_{12}$	$0.307^{+0.018}_{-0.016}$
$sin^2\theta_{23}$	$0.386^{+0.024}_{-0.021}(0.392^{+0.039}_{-0.022})$
$sin^2\theta_{13}$	$0.0241 \pm 0.0025(0.0244^{+0.0023}_{-0.0025})$

Double beta decay experiments can shed light on absolute scale of masses

of neutrinos. When mediated by virtual exchange of massive Majorana neutrino the $0\nu\beta\beta$ rate can be expressed as

$$\frac{1}{T^{0\nu}_{1/2}} = G^{0\nu} \mid M^{0\nu} \mid^2 \frac{\mid m_{ee} \mid^2}{m_e^2} \tag{1.19}$$

where $T^{0\nu}_{1/2}$ is the decay half life and m_e is mass of an electron. The $G^{0\nu}$ is the phase space integral and is exactly calculable while the calculation of nuclear matrix element $\mid M^{0\nu} \mid^2$ is strongly dependent on the nuclear model used for evaluation. The quantity $\mid m_{ee} \mid$ is a linear combination of neutrino mass eigenstates and is defined as

$$\mid m_{ee} \mid = \mid \sum_k U^2_{ek} m_k \mid \tag{1.20}$$

where U_{ek} are elements of PMNS matrix 1.16. Given the present experimental results of the parameters governing neutrino oscillation (Table 1.2), the current bound on m_{ee} as function smallest neutrino mass is shown in Figure 1.2. Important constraints on the neutrino mass can be derived from the $0\nu\beta\beta$ decay experiments. If the neutrinos are Majorana particle then a negative result in the range of 10 - 100 meV would rule out the inverted hierarchy scenario. Also, in case the next generation of oscillation experiments suggests inverted ordering of neutrino mass then a non-observation of $0\nu\beta\beta$ would indicate that neutrinos are necessarily Dirac particles.

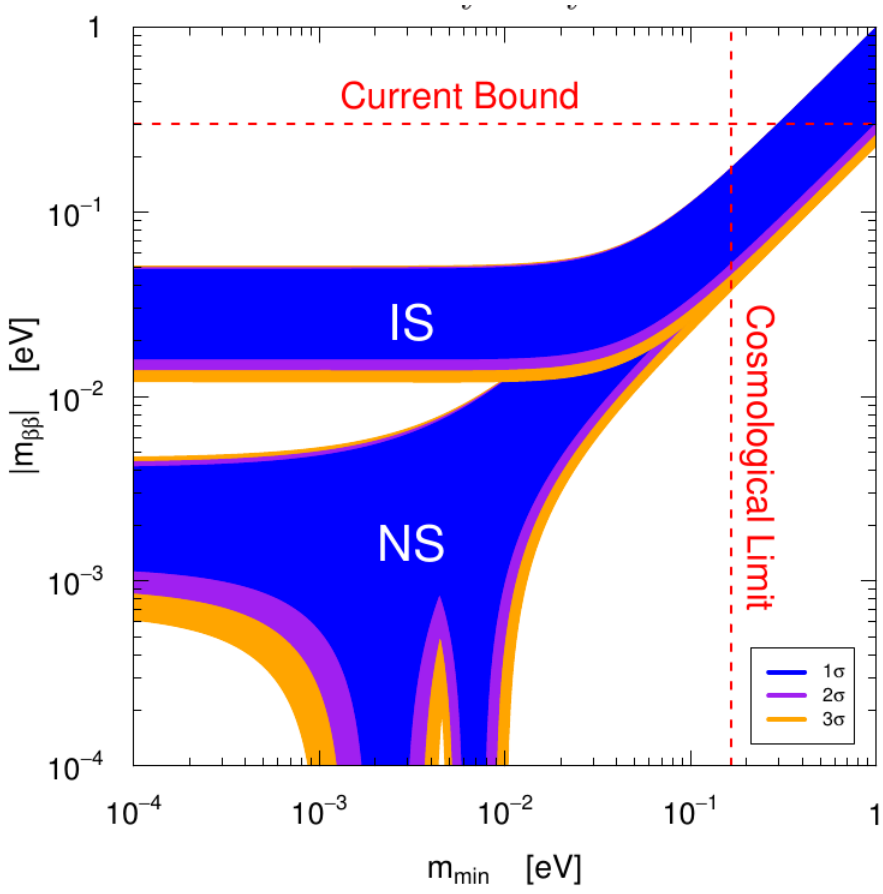

Figure 1.2: Majorana neutrino mass as a function of the smallest neutrino mass in the normal hierarchy (NS) and in the inverted hierarchy scenario (IS) (Figure from [25])

1.3 Experimental searches for $0\nu\beta\beta$ decay

A peak in the sum energy spectrum of the two electrons emitted in Eqn.1.4 at the Q value of the nuclear transition will serve as an experimental signature for observation of $0\nu\beta\beta$ decay. If a peak is observed then for the

measuring time $t \ll T_{1/2}^{0\nu}$ the half-life can be written as

$$T_{1/2}^{0\nu} = ln2 \, \frac{N_a \, t \, \varepsilon}{N_{0\nu\beta\beta}} \tag{1.21}$$

where $N_a = i \, N_A(M/A)$ is the number of $\beta\beta$ candidate atoms (N_A and i are Avogadro's number and isotopic abundance, respectively), ε is the detection efficiency and $N_{0\nu\beta\beta}$ is the number of observed $0\nu\beta\beta$ events. This is true only if the energy spectrum has zero background in the region of interest. If no $0\nu\beta\beta$ peak is observed in the presence of constant background B (i.e., it scales linearly with time), the sensitivity of an experiment is defined as the process half-life corresponding to the signal that could be mimicked by a background fluctuation of a chosen confidence level.

$$T_{1/2}^{0\nu}(n_\sigma) = \frac{ln2}{n_\sigma} \, \frac{N_A \, i \, \varepsilon}{A} \, f(\Delta E) \sqrt{\frac{M \, t}{B \, \Delta E}} \tag{1.22}$$

where n_σ is the chosen significance level expressed in numbers of Gaussian standard deviations and B is expressed in units of counts/year/kg/keV. The $f(\Delta E)$ is the fraction of signal events in the window of ΔE around the Q value. It is evident from Eqns. 5.3 and 5.1 that a $0\nu\beta\beta$ experiment must have the following characteristics to achieve best sensitivity for $\mid m_{ee} \mid$.

- Very large active mass of isotopic candidate ($\sim$ 100 Kgs to a ton)

- A higher natural isotopic abundance is desirable as the cost of isotopic enrichment could be significant for most of the candidates.

- Long measurement time with very low background rate.

- High efficiency and good energy resolution near the end point energy.

- The decay transition should have a high Q value since the decay rate (in particular the phase space factor in Eqn. 5.3) is proportional to Q^5. Candidates with Q value more than 2 MeV are preferred. Also, the interference from natural radioactive background is less at higher energies. The 2615 keV line of ^{208}Tl is the most energetic γ line visible in the ambient background radiation spectra. Above this the background due to gamma rays is negligible and can come only from rare decays or cosmogenic activation of the material. From these perspectives candidates with Q value more than 2615 keV are more desirable.

- An accurate evaluation of nuclear matrix element ($M^{0\nu}$) for $\beta\beta$ candidate. Any uncertainty in nuclear matrix element calculation will correspond to large uncertainty in $\mid m_{ee} \mid$.

There are 35 $\beta\beta$ candidate isotopes ([26]) out of which only 11 have a Q value higher than 2 MeV and are being explored by different experimental groups around the world. Almost all of them rely on the direct observation of both the electrons emitted in the decay process. The experimental

approaches can be classified in two categories depending on the detection technique used.

- **Homogeneous detectors (source and detector are same)**: The source is internal to the active volume of the detector. In this case only the sum energy of the two emitted electrons is detected. The calorimeter implementation can be a semiconductor, liquid scintillator, and cryogenic bolometer. The advantage of this approach is that the calorimeter can have large target mass with high efficiency of β detection. In addition, bolometers and semiconductors offer very high energy resolution.

- **Inhomogeneous detectors (source and detector are separate)**: These are essentially tracking detectors where a thin foil of $\beta\beta$ candidates is kept between two tracking detectors. In this method the tracking detectors determines the energy and direction of individual electrons emitted in the process. These detectors can be limited by poor energy resolution, low efficiency and self-absorption of the electron in source mass. However, they offer considerable background reduction due to coincidence measurement of both the electrons. Also, the angular correlation of the electrons can be measured which may provide insight into the underlying mechanism of neutrinoless double beta decay.

Some of the ongoing and planned $0\nu\beta\beta$ decay experiments have been listed in Table. 1.3 along with their detection techniques. Till now, $0\nu\beta\beta$

Table 1.3: Ongoing and proposed $0\nu\beta\beta$ experiments along with their detection technique.

Experiment	Isotope	Technique
CANDLES [27]	^{48}Ca	Solid Scintillator
GERDA [28]	^{76}Ge	Semiconductor
MAJORANA [29]	^{76}Ge	Semiconductor
SuperNEMO [30]	^{82}Se	Tracking + Calorimeter
LUCIFER [31]	^{82}Se	Cryogenic Bolometer + Scintillator
AMoRE [32]	^{100}Mo	Cryogenic Bolometer + Scintillator
MOON [33]	^{100}Mo	Tracking + Scintillator
COBRA [34]	^{116}Cd	Semiconductor
$CdWO_4$ [35]	^{116}Cd	Solid Scintillator
CUORE [36]	^{130}Te	Cryogenic Bolometer
EXO-200 [37]	^{136}Xe	Tracking
KamLAND-Zen [38]	^{136}Xe	Liquid Scintillator
SNO+ [39]	^{150}Nd	Liquid Scintillator

decay has not been seen in any of the isotopes and only a lower limit exists for the respective half-lives(Table 1.4). There has been a claim of a measurement of the $0\nu\beta\beta$ decay of ^{76}Ge with $T_{1/2}^{0\nu-exp} = 1.19^{+1.00}_{-0.17} \cdot 10^{25}$ yrs [40]. However, this claim stands unverified, is controversial [41, 42] and there is no consensus among the scientific community about its validity. While the recent results from GERDA-I [43] clearly disfavors the claim made in [40], the only certain way to confirm or refute it is with additional sensitive experiments.

Table 1.4: $\beta\beta$ candidates with Q values greater than 2 MeV. The SM process of $2\nu\beta\beta$ decay has been observed in most of the candidates while only limits exists for $0\nu\beta\beta$ process.

Isotope	Q_{value} (keV) [44]	Nat. Abun. (%)	$T^{2\nu}_{1/2}$ (yrs) [26, 45]	$T^{0\nu-exp}_{1/2}$ (yrs) [26, 46]
^{48}Ca	4362 ± 0.84	0.187	$4.4^{+0.6}_{-0.5} \cdot 10^{19}$	$> 1.4 \cdot 10^{22}$
^{76}Ge	2039.006 ± 0.050	7.73	$1.6^{+0.13}_{-0.1} \cdot 10^{21}$	$> 2.1 \cdot 10^{25}$ [43]
^{82}Se	2997.9 ± 0.3	8.73	$0.92 \pm 0.07 \cdot 10^{20}$	$> 3.6 \cdot 10^{23}$
^{96}Zr	3347.7 ± 2.2	2.80	$2.3 \pm 0.2 \cdot 10^{19}$	$> 9.2 \cdot 10^{21}$ [47]
^{100}Mo	3034.40 ± 0.17	9.82	$7.1 \pm 0.4 \cdot 10^{18}$	$> 1.1 \cdot 10^{24}$ [48]
^{110}Pd	2017.85 ± 0.64	11.72	$> 6.0 \cdot 10^{16}$	$> 6.0 \cdot 10^{16}$
^{116}Cd	2813.50 ± 0.13	7.49	$2.85 \pm 0.15 \cdot 10^{19}$	$> 1.7 \cdot 10^{23}$
^{124}Sn	2292.64 ± 0.39	5.79	$> 1.0 \cdot 10^{17}$	$> 2.0 \cdot 10^{19}$ [49]
^{130}Te	2527.518 ± 0.013	34.08	$6.9 \pm 1.3 \cdot 10^{20}$	$> 2.8 \cdot 10^{24}$ [50]
^{136}Xe	2457.83 ± 0.37	8.86	$2.20 \pm 0.06 \cdot 10^{21}$	$> 1.9 \cdot 10^{25}$ [51]
^{150}Nd	3371.38 ± 0.20	5.64	$8.2 \pm 0.9 \cdot 10^{18}$	$> 1.8 \cdot 10^{22}$

The best present limits on $\mid m_{ee} \mid$ are presented in Table 1.5. The spread in the values of $\mid m_{ee} \mid$ is due to the uncertainty in calculation of $M^{0\nu}$ using different nuclear models.

Table 1.5: Best present results on $0\nu\beta\beta$ decay [45]

Experiment	Isotope	$\mid m_{ee} \mid$ (eV)
GERDA-I	^{76}Ge	$< 0.25 - 0.62$
NEMO-3	^{100}Mo	$< 0.34 - 0.87$
CUORICINO	^{130}Te	$< 0.31 - 0.76$
KamLAND-Zen	^{136}Xe	$< 0.14 - 0.34$

1.4 Cryogenic Bolometer for $0\nu\beta\beta$ in ^{124}Sn

A feasibility study to search for $0\nu\beta\beta$ in ^{124}Sn at the upcoming underground facility, India based Neutrino Observatory (INO) has been initiated [52]. The TIN.TIN experiment (The INdia-based TIN detector) will be housed at INO, an underground facility with $\sim$ 1000 m rock cover all around [53]. The ^{124}Sn has moderate isotopic abundance $\sim$5.83% and a reasonably high Q value of 2.292 MeV. Cryogenic bolometers, with excellent energy resolution and high sensitivity, are well suited to search for $0\nu\beta\beta$. Tin becomes superconducting below 3.7 K and at T$<$100 mK its specific heat has only lattice contributions and can be used to make a bolometric detector. Very small size ($\sim$ mg) Sn bolometers have been found to give the best energy resolution at sub-kelvin temperature [54, 55] as compared to the next best Si(Li) detectors viz. $\sim$3-4 eV vs. 150 eV for Fe K-Xray.

1.4.1 Bolometer Principle

A bolometer is a low temperature detector where the energy of impinging radiation is converted into phonons leading to a measurable temperature rise. When a particle traverses through the crystal (absorber) it interacts with the lattice and a large fraction of the energy is deposited in the crystal as heat. The deposited energy raises the temperature of the crystal and the

heat signal is measured by an appropriate sensor. A simple schematic for the calorimeter is shown in Figure 1.3 where a crystal absorber with heat capacity C is connected to a bath at temperature T_0 through a weak heat link with a conductivity K.

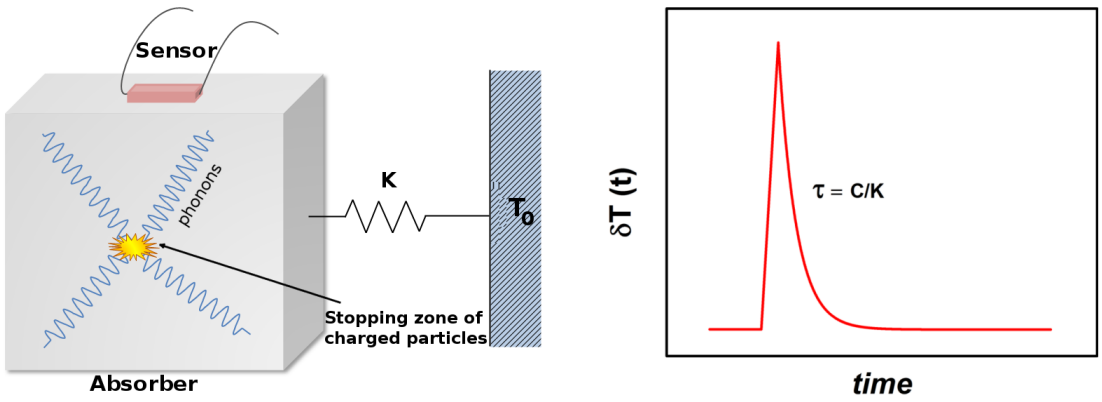

Figure 1.3: A simple schematic of a bolometer detector (left). The temperature response of the bolometer is shown on right.

When a particle of energy ΔE heats this crystal after thermalization of the phonons the temperature of the crystal rises to $T_0 + \delta T$ where

$$\delta T = \frac{\Delta E}{C}. \tag{1.23}$$

For small energy deposition one can assume that

$$\delta T = \mid T(t) - T_0 \mid \ll T_0 \ \forall\, t \ \ \Rightarrow C, G = constant. \tag{1.24}$$

The system then returns to equilibrium temperature T_0 with a time constant $\tau = C/K$ according to

$$\delta T(t) = \frac{\Delta E}{C} \cdot exp(-t/\tau). \tag{1.25}$$

As is evident from the above expressions the absorber, temperature sensor and the thermal link constitute the three main components of the bolometer.

Absorber Crystal

The heat capacity of the absorber is the most crucial aspect of a bolometer as a small heat capacity will reflect in a higher pulse amplitude and lower decay time to achieve thermalization. Dielectric and diamagnetic crystals or superconducting metals well below its transition temperature are suitable candidates for bolometer absorbers as their heat capacity varies as T^3 at sufficiently low temperatures. Since the heat capacity is also proportional to the mass of absorber, depending on the type of radiation to be detected, the mass of the calorimeters ranges from a few mg to a kg. Large size bolometers with mass ranging from several kilograms to a ton have found attractive application in rare event studies like Dark Matter search [56, 57], Neutrinoless Double Beta Decay [58, 59] etc.

Tin has been chosen as the candidate for TIN.TIN. As evident from above discussion, the specific heat of the detector is the most important point for signal formation. The heat capacity of a material depends on the total number of degrees of freedom within the crystal and can be written as sum of three terms

$$C = C_e + C_l + C_m \tag{1.26}$$

where C_e, C_l and C_m denote the contribution from electronic, lattice and magnetic heat capacity. In the absence of magnetic impurities or any nuclear moments and spin degree of freedom, the heat capacity of a superconductor will have only contributions from electronic and lattice heat capacity. The BCS theory predicts an exponential behavior for electronic heat capacity as the electrons start building up Cooper pairs in the superconducting phase for $T \ll T_c$:

$$C_e = 9.17 \cdot \gamma T_c \cdot e^{-\frac{1.5T_c}{T}} \tag{1.27}$$

The lattice contribution can be estimated from the Debye theory of solid at low temperature ($T \ll \Theta_D$)

$$C_l = \frac{12\,\pi^4}{5} \cdot N_A k_B \cdot \left(\frac{T}{\Theta_D}\right)^3 \tag{1.28}$$

The electronic heat capacity decays exponentially and at $T \ll T_c$ it is possible to use superconductors as absorber in low temperature calorimeters.

Therefore, Tin ($T_c = 3.7$ K and $\Theta_D = 200$ K) is an ideal candidate for bolometer absorber when operated below 100 mK.

The distribution of the energy during the thermalization process is well summarized by the Andersen's scheme [60] shown in Figure 1.4 below. The energy of the incident radiation downgrades to heat through two main channels: nuclear and electronic. The diagram is simplified in the sense that

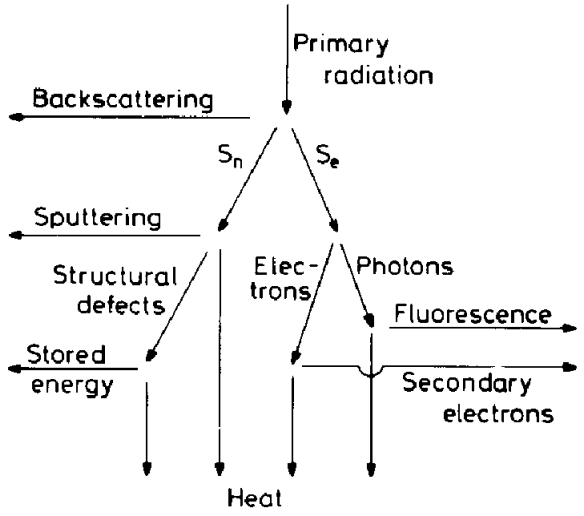

Figure 1.4: Andersen's scheme of thermalization inside a calorimeter. Only fraction of the energy appearing as heat at the bottom of the diagram contributes to the signal.

energy from the nuclear channel may flow back in the electronic channel through ionization and excitation caused by recoiling atoms. Also, energy may flow back and forth between the photon and electron branches. However, there is no coupling of the electronic side to the nuclear channel.

Hence, not all the energy of an incident particle stopped in the detector appears as heat and only the fraction of the energy appearing as heat at the bottom of Figure 1.4 contributes to the signal. This fraction of the energy, available as heat, is dependent on the type of incident radiation and the calorimeter material as well as energy itself. The energy resolution of the detector is determined by the fraction of heat signal detected.

Temperature sensor

A temperature sensor can be any device which can detect the small variations of temperature and should be able to generate an electrical signal proportional to the energy contained in the absorber. Different kind of sensors exists out of which NTD-Ge, Transition edge sensors (TES), Metallic magnetic calorimeters (MMC) and Microwave Kinetic Inductance Detectors (MKID) are mostly used by experimental groups around the world. While MMC and MKIDS are relatively new technologies, the fabrication techniques of NTD-Ge and TES are well developed [61]. Both NTD and TES are resistive thermistors whose resistance as a function of temperature has a steep slope. In this way a little variation of temperature could generate a significant and measurable variation of resistance. Presently NTD-Ge

sensors are used for the R&D of TIN.TIN detector. Compared to the conventional metallurgical methods, neutron transmutation doping yields good uniformity and is found to show good reproducibility [62, 63].

Thermal Link

The thermal link connects the calorimeter absorber to the heat sink. It mainly depends on choice of material which is used to hold the absorber crystal to the thermal bath. Together with the system heat capacity it influences the time response of the bolometer. The thermal conductance of the heat link should be weaker than thermal conductance of the energy absorber. Use of conductor and magnetic materials should be avoided, as part of the thermal link contributes to the overall heat capacity of the calorimeter. From point of view of rare event studies it is further necessary that the support structure are of high radio-purity. Teflon fulfills most of the above criteria and has been extensively used as weak thermal link by experiments working with massive calorimeters.

1.5 Resolution of a bolometer

A bolometer can be considered as a canonical system that is connected to a large ensemble at a fixed temperature T_0. In this case the mean energy

of the bolometer can be given as (with $\beta = 1/k_B T$)

$$U \equiv \langle E \rangle \;=\; \frac{\sum E_r e^{-\beta E_r}}{\sum e^{-\beta E_r}} \tag{1.29}$$

Using the above relation it is easy to follow the energy fluctuation inside the absorber

$$\begin{aligned} \langle (\Delta E)^2 \rangle \equiv \langle E^2 \rangle - \langle E \rangle^2 &= -\left(\frac{\partial U}{\partial \beta}\right) \\ &= k_B T^2 \left(\frac{\partial U}{\partial T}\right) = k_B T^2 C \end{aligned} \tag{1.30}$$

where we have used the fact that

$$\left(\frac{\partial U}{\partial T}\right) = \left(\frac{\sum E_r e^{-\beta E_r}}{\sum e^{-\beta E_r}}\right)^2 - \left(\frac{\sum E_r^2 e^{-\beta E_r}}{\sum e^{-\beta E_r}}\right) \tag{1.31}$$

Hence, in the absence of incoming external energy $\Delta E = \sqrt{k_B T^2 C}$ is the limit of the measurement for the bolometer.

If phonons are the only modes of excitation in the crystal at low temperature then it is simpler to physically understand the above expression. If $\varepsilon_p h$ is the average energy of the phonons excited in the absorber when a radiation falls on it, then the total number of phonons in the crystal at thermal equilibrium can be estimated as

$$N_p h = \frac{C \cdot T}{\varepsilon_p h} = \frac{C \cdot T}{k_B \cdot T} = C/k_B \tag{1.32}$$

Assuming that the thermodynamic fluctuations of the number of thermal phonons exchanged with heat bath through conductance K follows a Poisson distribution

$$\Delta N_{ph} = \Delta N_{ph} \cdot k_B T = \sqrt{N_{ph}} \cdot k_B T = \sqrt{k_B T^2 C} \tag{1.33}$$

which is identical to the expression derived in Eqn. 1.30. It can been seen that for a good performance of bolometer the absorber crystal should have very small heat capacity and should be operated at extremely low temperatures to keep the fundamental fluctuation noise to its minimal. However, for all practical purposes the performance of bolometer is not limited by its fundamental fluctuation noise. For example, for 10 gm of Tin operated at 10 mK the fundamental limit to the energy resolution would be $\sim$ 1 eV (at 100 mK, $\Delta E \sim$ 320 eV). The resolution of a bolometer is far more severely affected by the noise arising from the cryogenics, electronics and read out setup and is independent of the energy of the incident radiation.

This thesis describes the endeavours and R&D work towards cryogenic Tin bolometer development.

Chapter 2

Cryogen Free Dilution Refrigerator for TIN.TIN

2.1 Introduction

Large size cryogenic bolometers with mass ranging from several kilograms to a ton have found attractive application in rare event studies like Dark Matter search, Neutrinoless Double Beta Decay experiments etc. Continuous cooling of these bolometers below 1K is achieved using dilution refrigerators. Large detector masses put extremely stringent conditions on the cooling power of these dilution refrigerators.

This chapter describes the design and performance of a custom built M/s. Leiden Cryogenics make CFDR-1200 for the development of Sn prototype bolometer. The CFDR-1200 is a combination of a Pulsed Tube Cryocooler with a $^3He/^4He$ dilution unit, equipped to reach temperature below 10 mK.

Given the long time scale of $0\nu\beta\beta$ experiment and remote locations of underground laboratories, the choice of a cryogen free dilution refrigerator instead of conventional wet system (which requires liquid helium supply), is imperative. Also, the experimental space in the cryogen free dilution refrigerator can be increased as much as needed as there are no size limitations due to Helium dewars. Furthermore, the cryogen free dilution refrigerator minimizes the vibrations originating from 1K pot used in wet dilution refrigerators [64].

2.2 Principle of ^{3}He/^{4}He Dilution refrigerator

The dilution refrigerator is the workhorse in the millikelvin temperature range. First proposed by H. London in 1951, the dilution refrigerator was experimentally realized in 1964 by Das *et. al.* [65]. It takes advantage of the low temperature properties of ^{3}He/^{4}He mixture. As shown in the phase diagram in Figure 2.1, the mixture undergoes a spontaneous phase separation to form a ^{3}He-rich phase (concentrated phase) and a ^{3}He-poor phase (dilute phase, ^{4}He-rich) when cooled below T_λ = 870 mK. In the dilute phase there is a minimum solubility of $\sim$6.5% even as the temperature approaches absolute zero. ^{4}He atoms are superfluid at this temperature and have zero viscosity, zero entropy and infinite thermal conductivity. On the other hand ^{3}He does not become superfluid and behaves like a perfect Fermi gas in

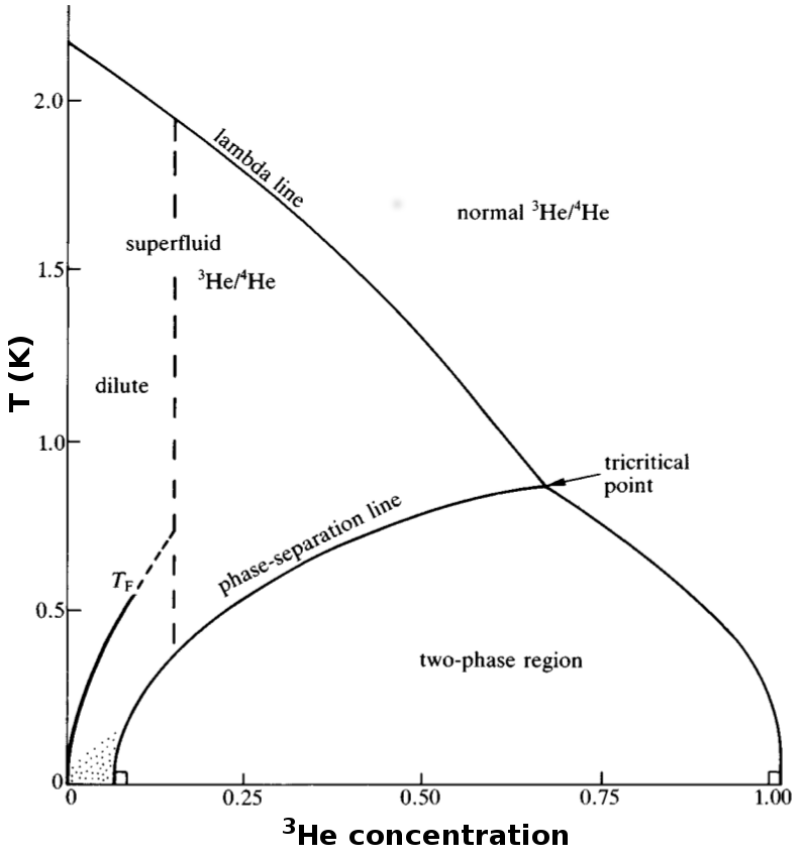

Figure 2.1: Phase diagram of ^{3}He/^{4}He mixture at zero pressure. Figure from [66]

an inert background ^{4}He quantum solvent. Since the ^{3}He vapor pressure is much higher than the ^{4}He vapor pressure, by pumping on the dilute phase (^{4}He-rich phase) it is possible to remove mostly ^{3}He (a move to the left off the equilibrium line in the diagram), destroying the equilibrium. To restore the equilibrium, ^{3}He crosses the phase boundary from the ^{3}He-rich side to the ^{4}He-rich side. The process is endo-thermal and removes heat from the ^{3}He/^{4}He interface, thereby achieving cooling. At low temperatures ^{3}He atoms in both concentrated and dilute phase behave as Fermi liquids whose

entropies are proportional to temperature.

$$S_C = \gamma_C \cdot T, \tag{2.1a}$$

$$S_D = \gamma_D \cdot T, \tag{2.1b}$$

where γ_C and γ_D are coefficients of heat capacity of ^{3}He in the concentrated phase and the dilute phase, respectively. As mentioned above, cooling takes place in the mixing chamber of the dilution refrigerator when the ^{3}He atoms move from the low entropy concentrated phase into the high entropy dilute phase. The cooling power $\dot{Q}$ of the refrigerator is therefore proportional to the molar circulation rate ($\dot{n}$) of ^{3}He and is given by

$$\begin{aligned} \frac{\dot{Q}}{\dot{n}} &= T_m \cdot \Delta S \\ &= (\gamma_D - \gamma_C) \cdot T_m^2, \end{aligned} \tag{2.2}$$

where T_m is temperature of the mixture. The cooling results according to the enthalphy difference of the two phases.

2.3 Design of Cryogen Free Dilution Refrigerator for TIN.TIN

It is envisaged that the prototype stage of TIN.TIN would consist of an array of $\sim$ 30 Tin (Sn) crystals (natural/enriched $\sim$ 3x3x3 cm^3 each) arranged in a tower geometry with corresponding readout sensors (the size

optimization of crystals is described in Chapter 4). Since the sensitivity of $0\nu\beta\beta$ experiment is crucially dependent on the minimization of background radioactivity, it is essential that the material surrounding the detector elements should be of high radio-purity. In addition, a bulk shielding is highly desirable inside the cryostat to suppress the background events arising from the materials used for cryostat construction [67]. Therefore, a provision for additional low activity shielding inside the cryostat is also incorporated in the design. The dilution refrigerator has a cylindrical sample space of 300 mm x 300 mm available below the Mixing Chamber (MC) which is inside the inner most 50 mK shield and can support a total mass of $\sim$ 100 kgs (Sn detector and $\sim$ 5cm thick low activity lead shield).

Figure 2.2 shows a complete schematics of the dilution unit. The dilution unit consists of a Still, a 50 mK cold plate, a MC and a series of heat exchangers, integrated with a pulsed tube cooler [68]. The dilution unit is protected against radiation heat load by means of shields at 50K, 3K, Still and 50 mK. The 50K and 3K stage shields are fabricated from aluminum, wrapped in multi layer mylar insulation and are cooled by the two stages of the pulsed tube cooler. The shields at the Still and the 50 mK stage are made of gold plated copper and are cooled by the dilution refrigerator. The 3K shield also serves as an inner vacuum chamber (IVC). The external vessel of the cryostat which acts as the outer vacuum can (OVC) is at

room temperature. A charcoal loaded cryo-pump is mounted on the 50K and the 3K stage to adsorb any residual gas in the OVC and the IVC, for minimizing the heat load due to gas conduction. The cooling in the pulsed

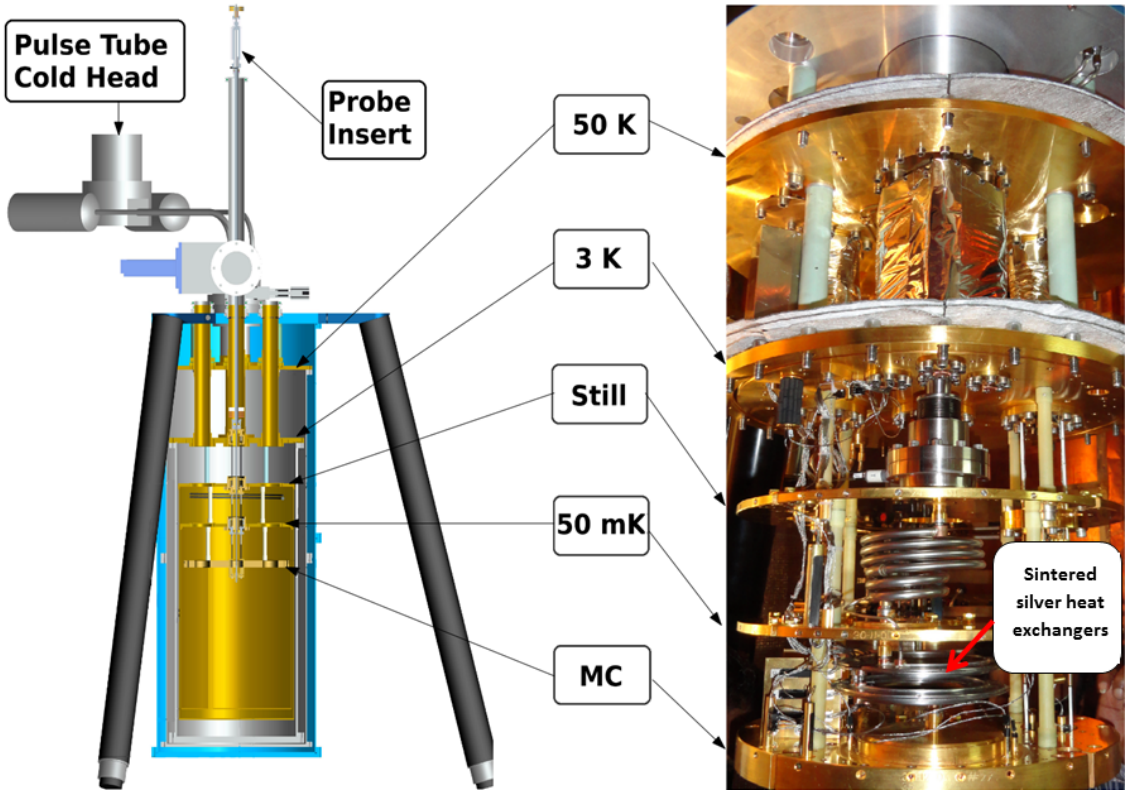

Figure 2.2: Schematics of CFDR-1200 dilution unit at TIFR. The image on right shows the actual unit.

tube is achieved using a closed loop Helium expansion cycle. The pulsed tube cooler consists of a compressor unit and a Cold Head unit. The compressor unit compresses pure helium (^{4}He) gas and the heat of compression is removed via a water cooled heat exchanger. The compressed Helium is

then fed to the Cold Head where adiabatic expansion of Helium takes place allowing the system to cool down to cryogenic temperatures. The pulsed tube cooler in this system is Cryomech-PT415 with a remote valve motor option [69] and has a typical cooling capacity of 1.5 W at 4.2K. The valve control unit, which incorporates a stepper motor and controls the gas flow, is detached from the PT-cooler by a 65 cm flexible single hose and is mounted on a vibration dampner. This reduces the vibrations transmitted to the cryostat. The valve unit is electrically isolated from the cryostat by means of a nylon insulator. The valve is driven by a stepping motor driver that sends square pulses resulting in sharp steps of current through the motor windings and a jerky rotation. The stepper motor driver supplied by Cryomech hence is far from ideal, generating vibrations in the stepper motor at 140 Hz and higher harmonics. The 140 Hz vibrations are a result of the design of the stepper motor. These vibrations have been minimized by using a linear microstepping motor driver, which linearly ramps current between microsteps instead of changing it abruptly. The cold head motor has been modified to be driven by a custom LNX-G linear motor drive (Precision Motion Control, Inc.) which reduces the amplitude of 140 Hz vibrations. The changeover from Cryomech motor driver to LNX-G linear motor drive is done below

100 mK. The compressor is installed outside the experimental room to reduce acoustical noise. The cold head is connected to the compressor by means of two 20 m long flexible lines.

For achieving a temperature lower than 3K, the ^{3}He / ^{4}He mixture is condensed using a Joule-Thomson heat exchanger which is installed between the 3K plate and the Still. The amount of ^{3}He used in CFDR-1200 ($\sim$ 45 liters) is significantly smaller compared to ^{3}He used in the wet dilution refrigerator ($\sim$ 175 liters). A turbo molecular pump having a pumping speed of 1850 l/sec in series with a 800 m^3/hr dry roots pump constitute the pumping system on the Still line. This high throughput system provides substantial circulation rate (maximum flow rate of $\sim$1900 μmol/s beyond which the system becomes unstable). However, the excess flow rate is a source of heat load on the MC and limits the cooling power at very low temperature. A tube-in-tube continuous heat exchangers followed by a silver sinter heat exchanger is used between the Still and the 50 mK plate. The unit has a couple of continuous silver sinter heat exchanger installed between the 50 mK plate and the MC. The latest proprietary designs of Leiden Cryogenics have been used in construction of the MC, Still and heat exchangers to minimize the viscous heat load arising from a high flow rate. The high cooling power of CFDR-1200 is essential to cool the massive detector and shield elements to 10 mK.

The CFDR-1200 also has an additional option of a top-loading probe which gets connected to the mixing chamber. The probe has a cylindrical sample space of 40 mm x 80 mm and is inserted using one of the three clear shot tubes provided in the dilution unit which facilitates easy sample changes in the cold condition. The probe is thermally anchored at 3K, Still, 50mK and MC stage of the dilution unit to minimize the heat load due to conduction. However, it does introduce a small heat load on the main MC at the base temperature.

The Mixing Chamber temperature is monitored using a couple of calibrated Carbon Speer resistors and a paramagnetic Cerium Magnesium Nitrate (CMN) thermometer. A calibrated Platinum resistor (Pt-1000) is mounted on the MC to monitor the temperature above 10K, during the cool down. The resistance measurements are done using AVS-47B AC-resistance bridge while the inductance of the CMN is measured with a digital mutual inductance bridge. In addition to the standard diagnostic thermometry, the CFDR-1200 is equipped with readout wiring for up to 75 sensors (4 probe measurement). The wiring from room temperature to the 3K stage is done using shielded Phosphor Bronze wire while shielded NbTi wires are used from the 3K to the MC. The superconducting NbTi wires ensure that the thermal heat load on the MC due to the large number of wires is negligible. All 300 wires are connected with hermetically sealed connectors at the

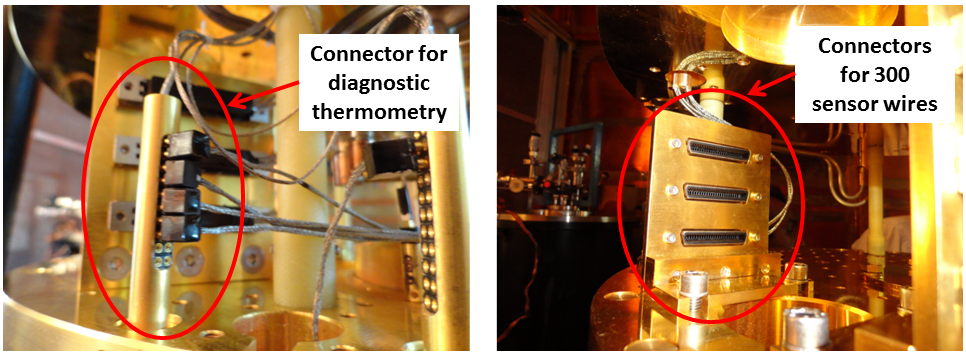

Figure 2.3: Connectors on Mixing Chamber for sensor readout.

50K stage and the 3K stage through two clear shot tubes. This also provides a possibility to mount a preamplifier stage for bolometer pulse processing at 50K, if needed in future. The operation of CFDR-1200 and diagnostic thermometry is controlled using M/s. Leiden's control program.

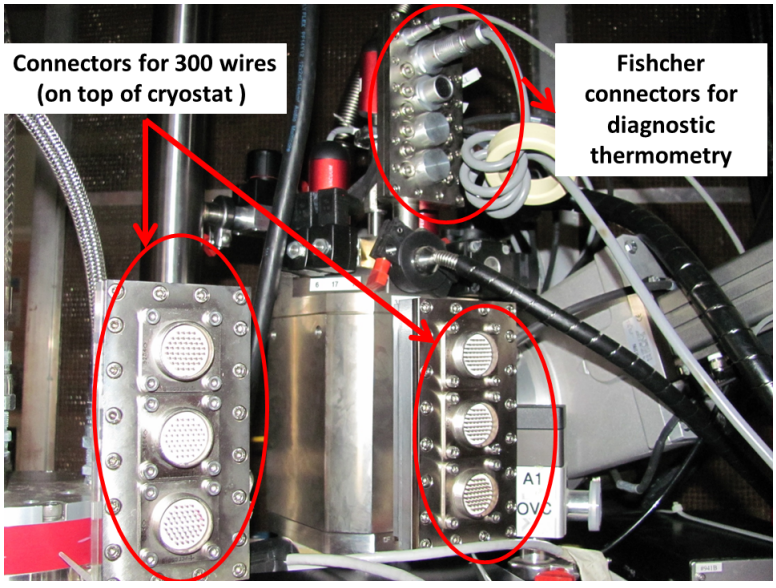

Figure 2.4: Connectors on top of cryostat for sensor readout.

The entire setup has been enclosed inside a specially constructed Faraday cage to minimize RF-EMI interferences. Copper (200μm) and galvanized iron (GI; 500μm) sheets/mesh were used for shielding. The total shielding effectiveness is a combination of absorption and reflection losses in copper/GI. Copper is used to shield against electric fields, plane waves and high frequency magnetic fields while GI effectively shields low frequency magnetic fields [70]. All the signal lines enter the enclosure though a pass-through panel. To reduce stray magnetic field the cryostat is further surrounded by 3 mm thick mild steel (MS) sheets from all sides. To avoid ground loops, the cryostat is electrically isolated from all gas circuit lines and pumping bellows using polymer rings and plastic clamps. The measurement units are kept outside the Faraday cage to minimize the effect of the irradiated EMI. The AC power lines for measurement units (resistance/inductance bridge etc.) are RF-filtered and a separate clean earth connection is used for them. The operations of the CFDR-1200 can either be semi-automatic or computer controlled. The Leiden's control program uses RS-232 serial protocol for computer interfacing and care has been taken to isolate the grounds of all the devices using RS-232 optical isolators. In case of power failure, the system is equipped with a back up power supply to keep the interface and safety valves working. The manufacturer has also

provided a high pressure safety (one way valve set at 1.8 bar) in the ^{3}He/^{4}He circulation circuit, which is connected to the ^{4}He storage.

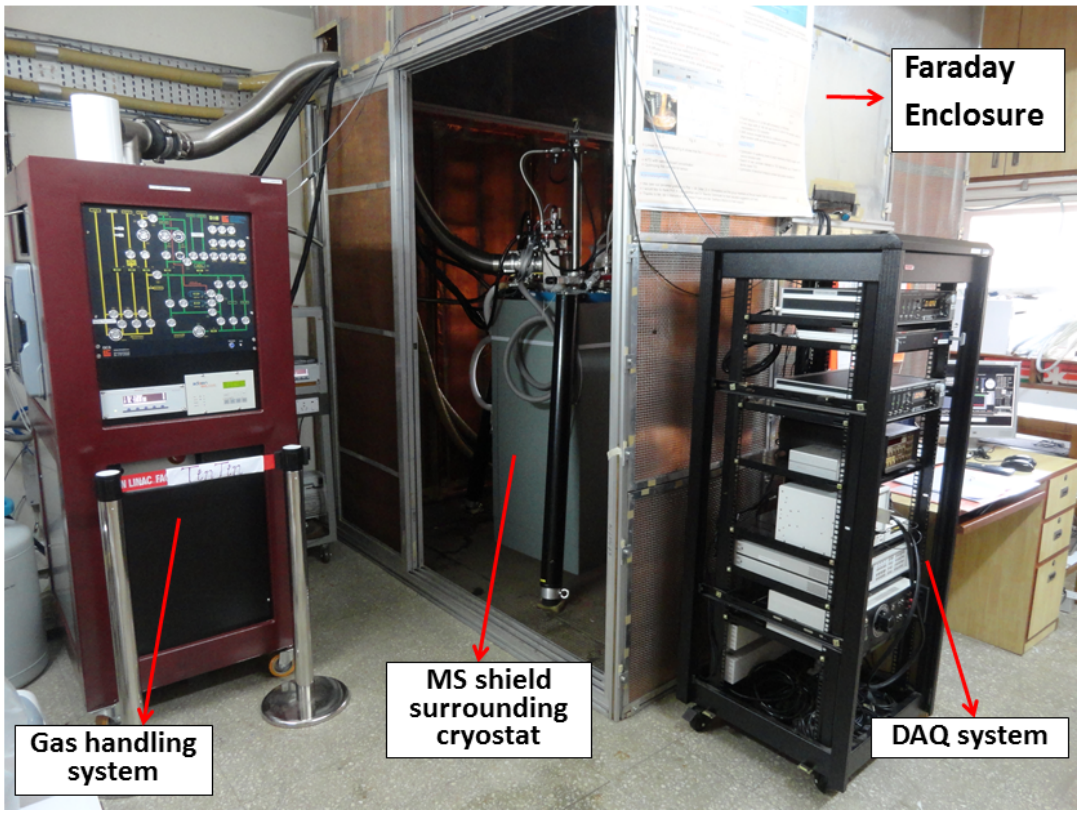

Figure 2.5: CFDR-1200 inside Faraday enclosure at TIFR, Mumbai.

The temperature calibration of the Carbon Speer resistor was verified against a Fixed Point Device (FPD1000). The FPD1000 uses the Meissner effect in superconducting samples of pure metals and alloys to indicate known transition temperatures and allows the calibration of other devices by interpolation. FPD1000 has 5 transition temperatures as shown in Table 2.1. Figure 2.6 shows the calibration of the Carbon Speer sensor (S1109) and the

Table 2.1: Materials used in the FPD and corresponding transition temperatures.

Compound	T_c (mK)
In	3300
Al	1175
Zn	840
Cd	520
$AuIn_2$	208
$AuAl_2$	161
Ir	97

CMN sensor (calibration as provided by the supplier) against the FPD1000 below 500 mK. It is clearly seen that the calibration of Carbon Speer sensor is reliable in the temperature range of interest. There is a large deviation of the calibration of the CMN sensor, above 150mK, from the actual temperature indicated by the FPD1000. The CMN sensor was recalibrated using the FPD1000. The CMN is a dilute paramagnetic salt and its magnetic susceptibility is related to the temperature through the Curie-Weiss law. The mutual inductance of a CMN sensor varies as,

$$M = M_0 + \frac{\lambda}{T} \tag{2.3}$$

where λ is the Curie constant. A straight line fit of the mutual inductance against inverse of the temperature with three points (at T_c = 97, 161 and 208 mK) is good enough to determine the constants M_0 and λ of Eq. 2.3 accurately. It should be noted that the lowest transition point available on

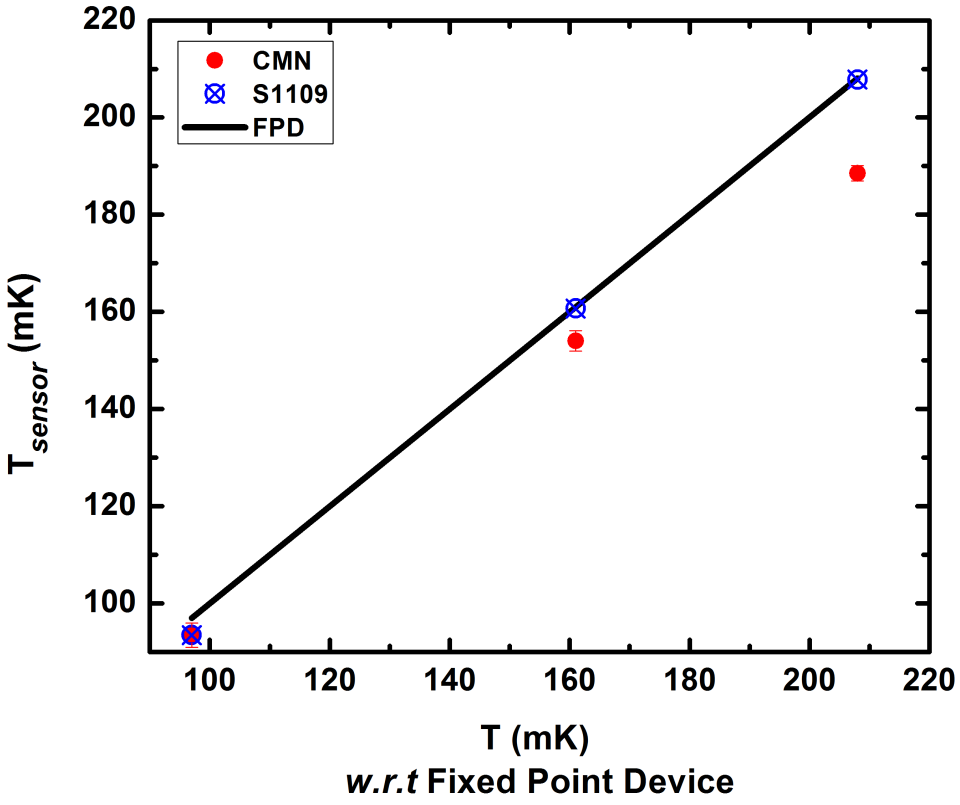

Figure 2.6: Calibration (as provided by the supplier) of the carbon speer resistor (S1109) and the CMN against the FPD. The original calibration of the CMN deviates appreciably at higher temperatures.

the FPD is only 97 mK. Below this the recalibrated CMN sensor is used for accurate measurement of the actual temperature.

The typical cool down time from the room temperature to the lowest base temperature is $\sim$ 24 hrs. The cool down from the room temperature to 77K is aided by a liquid nitrogen pre-cool to reduce the cool-down time. The warm-up time from the base temperature to the room temperature is close

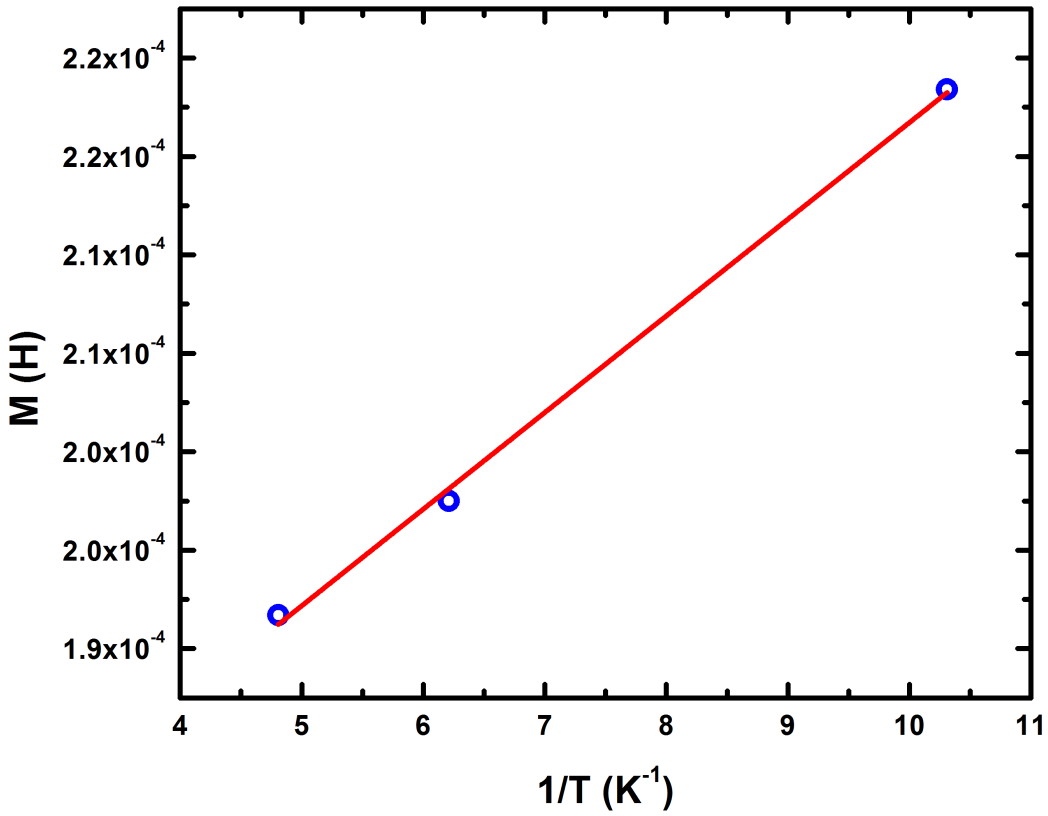

Figure 2.7: Recalibration of the CMN using the FPD. Data points correspond to T_c of 208, 161 and 97 mK, respectively.

to 2 days, which can be expedited by applying heater power at 50K stage and/or by adding dry Argon in the OVC as exchange gas.

2.4 Performance of the Cryogen Free Dilution Refrigerator

The cooling power of the CFDR-1200 has been measured for different ^{3}He flow rates and is shown in Figure 2.8. The measurements were done

with the probe inserted in the system and hence, the lowest temperature reached was 12 mK. The temperature on the MC was controlled by sup-

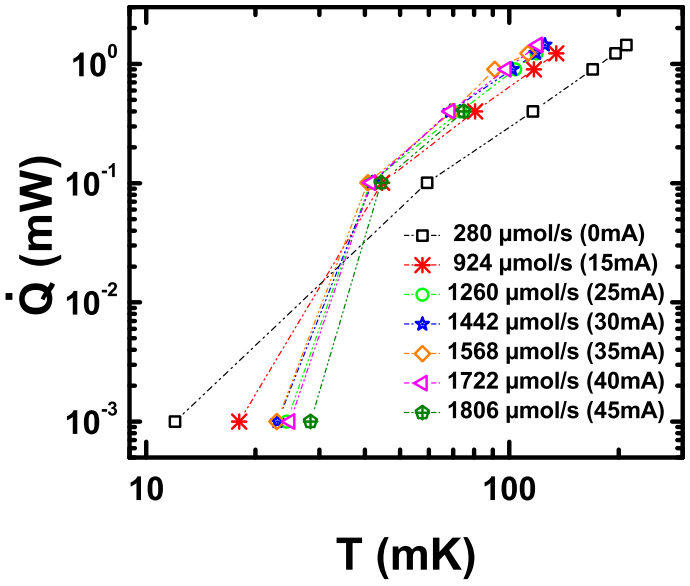

Figure 2.8: The measured cooling power for different flow rates as a function of T. Numbers in parenthesis indicate the Still heater current. An offset of 1 μW has been included in $\dot{Q}$ for plotting on log scale.

plying current to a 100 Ω resistor on the MC plate. The flow rate was changed by applying 0 to 40 mA current to a standard 100 Ω heater inside the Still (I_{Still}). The lowest minimum temperature of 7$\pm$0.04 mK, measured with CMN thermometer, was achieved with a flow rate of 280 μmoles/sec ($I_{Still} = 0$ mA), without any external heat load on the system. The base temperature was stable within 0.5% over a period of 12 hours. Readings of all the calibrated sensors were consistent within $\pm$ 2 mK at the lowest

temperature. As shown in Figure 2.8, at temperatures above 50 mK there was a substantial gain in cooling power when the flow rate was increased from 280 μmoles/sec by increasing I_{Still}. However, the flow rate cannot be increased to very large values as the cooling power capacity suffers at very high flow rate. These measurements indicate an optimum flow rate of 1568 μmol/s for significant cooling power at temperatures above 50 mK. A cooling power of 1.4 mW was measured at 120 mK for the flow rate of 1568 μmoles/sec. It should be noted that the base temperature degraded from 12 mK to 30 mK as the flow rate was increased. Moreover, the system has two gas circuits lines for the ^{3}He/^{4}He mixture leading to the condenser line. Since the impedances of these lines are different, the flow rate could also be crudely controlled by circulating the gas through any one or both of these lines. The minimum base temperature was achieved when both the lines were open.

The cooling power of a dilution refrigerator is well studied in literature using standard thermodynamics, describing the ^{3}He/^{4}He mixture as a Fermi gas [71, 84], and is given by

$$\dot{Q_m} = \dot{n} \left(\left(\gamma_D - \gamma_C/2\right) T_m^2 - \left(\gamma_C/2\right) T_x^2 \right) \tag{2.4}$$

where, $\dot{Q_m}$ is the cooling power on MC, $\dot{n}$ is the circulation rate of ^{3}He, γ_D (107 $J/mole/K^2$) and γ_C (23 $J/mole/K^2$) are coefficients of heat capacity

of ^{3}He in dilute and concentrated phase, respectively. T_m is the temperature of the MC and T_x is the temperature of the last heat exchanger from which the ^{3}He gas exits before entering the MC. In an ideal heat exchanger of a dilution unit $T_x = T_m$ and the cooling power can be simplified as,

$$\dot{Q}_m = 84\,\dot{n}\,T_m^2 \;\; (J/mole/K^2) \tag{2.5}$$

Figure 2.9 shows the plot of $\dot{Q}/\dot{Q}_m$ as a function of T_m/T_b, where T_b is the lowest base temperature achieved. It can be seen that measured $\dot{Q}$ is consistent with Eqn.(2) for $T_m/T_b \geq 3$. For temperature $T_m < 3\ T_b$, the incoming ^{3}He flow acts like a heat load on the MC. Thus, the heat exchangers are unable to cool down the incoming ^{3}He to MC temperature T_m and the assumption $T_x = T_m$ is not valid. This has also been observed in conventional dilution refrigerators [73]. A more critical limit on the performance of the dilution refrigerator is determined by the intrinsic heat load on the MC. The base temperature achieved without the probe was 7 mK. However, when the probe was inserted into the MC the base temperature rose to 12 mK because of the heat load brought in by the thermal conduction of the probe. Takano [74] has suggested an empirical formula for the cooling power of a dilution refrigerator with an intrinsic heat leak, $\dot{Q}_0$ present in the system,

$$\dot{Q} = \dot{n}\,(\gamma_D - \gamma_C)\,(T_m^2 - T_0^2) \tag{2.6}$$

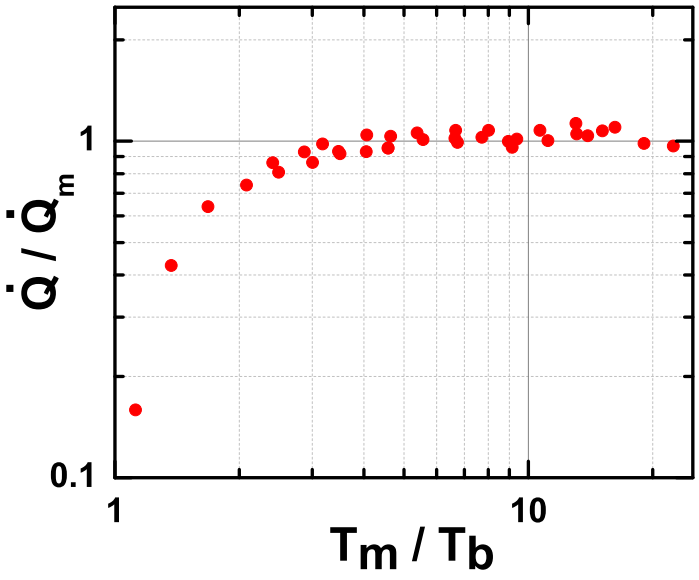

Figure 2.9: Normalized cooling power as a function of normalized temperature [see text for details].

where, T_0 is the lowest temperature in presence of the $\dot{Q}_0$. The relation between T_0 and the ultimate base temperature, T_b, is approximated by,

$$T_0{}^2 = T_b^2 + \frac{\dot{Q}_0/\dot{n}}{(\gamma_D - \gamma_C)} \tag{2.7}$$

The standing heat load of Probe insert $\dot{Q}_0$ in this case is estimated to be 3μW at 12 mK by fitting data with Eqn.(4) and is shown in Figure 2.10. This formula can also be employed to estimate the heat load when the larger detector array will be mounted on the MC.

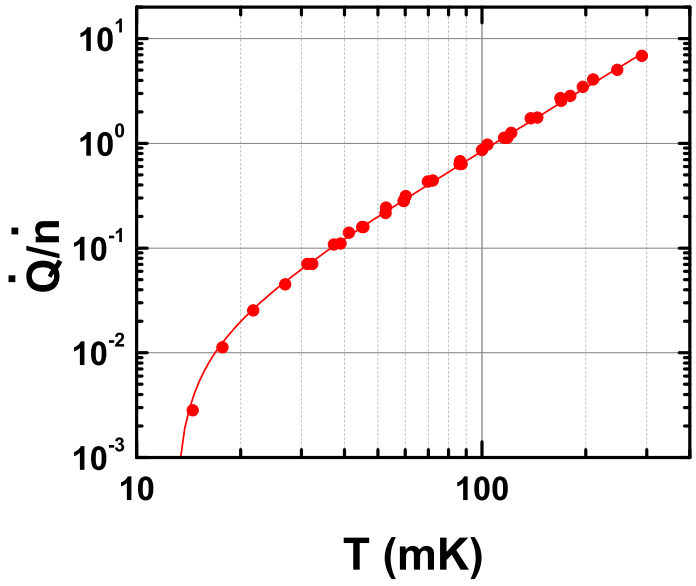

Figure 2.10: Cooling Power of CFDR-1200 in the presence of heat load. The solid line is the best fit to the data using Takano's formula [74] [see text for details].

2.5 Summary

A custom built cryogen free dilution refrigerator, CFDR-1200, with a high cooling power of 1.4 mW at 120 mK, has been successfully installed and tested at TIFR, Mumbai. The minimum base temperature of $<$10 mK has been measured using calibrated CMN thermometer and a carbon Speer resistor. The base temperature was stable within 0.5% over a period of 12 hours. After optimizing the operating conditions (flow rate), the performance of CFDR-1200 has been found to be consistent with the Takano's model for conventional refrigerator. The higher flow rate has resulted in a

greater cooling power with a significantly smaller quantity of ^{3}He as compared to standard wet dilution refrigerator. Care has been taken to minimize mechanical vibrations from the pulsed tube cooler and reduce radio frequency interference from the surroundings. The cooling power of the CFRD-1200 is regularly monitored after opening and re-assembling the Mixing chamber. The setup can be used for Sn bolometer development and other low temperature measurements.

Chapter 3

Heat Capacity Measurements

3.1 Introduction

The performance of bolometers as thermal radiation detectors is determined by its efficiency to measure the change in temperature against the thermodynamic energy fluctuation present in the system. As explained in Chapter 1, the heat capacity of the absorbing material is the most crucial aspect in a calorimetric particle detector construction as the intrinsic resolution of a calorimeter is strongly dependent on its heat capacity [75]. Bolometer absorbers when operated at temperature close to absolute zero have extremely small heat capacity and are sensitive to small amounts of energy deposited in a large absorber. In addition, bolometers provide a wide range of energy threshold, sensitivity to even non-ionizing particle events

and have found attractive applications in rare event studies. The heat capacities of various bolometer components (like thermistor, thermal links, etc) are also crucial to the performance of a calorimeter as they are strongly coupled to the absorber material.

Superconductors with high Debye temperatures are ideal candidates for calorimetric particle detectors as the electronic heat capacity falls off exponentially below their transition temperature T_C and only the lattice contribution to the heat capacity survives. At low temperature, detectors constructed using superconductors are expected to offer the energy resolution comparable to that of the diamagnetic insulating absorbers. Although large size calorimetric detectors constructed from diamagnetic insulators have found attractive applications [56, 57, 59, 76, 77], the use of superconducting absorbers has been limited only to microcalorimeters. It is reported that the spectral resolution of superconducting bolometers is limited by the incomplete thermalization of energy in the absorber materials. This has been attributed to energy trapping by quasiparticles with long lifetime in superconductors [78, 79]. In the low temperature limit, the average recombination lifetime of the quasiparticle is given by [80]

$$\tau_r = \frac{\tau_0}{\sqrt{\pi}} \left(\frac{k_B.T_c}{2\Delta}\right)^{5/2} \sqrt{\frac{T_c}{T}}\, exp\left(\frac{\Delta}{k_B T}\right) \tag{3.1}$$

where T_c and Δ are the critical temperature and the energy gap of the superconductor, respectively. The τ_0 is the characteristic electron-phonon interaction time and is material dependent. Contrary to the prediction of Eq. (3.1), recent measurements by Visser *et.al*. [81] in Aluminum show that the τ_r saturates to about 2.2 ms below 160 mK. Other superconductors such as Pb, Ta and Sn have much lower value of τ_0 ($<$ 2.5 ns [80]) compared to Al ($\tau_0 = 438$ ns). Here, because of a smaller τ_0, a lower saturation value of the quasiparticle lifetime τ_r is expected and a complete thermalization may be possible, which should lead to the improved energy resolution in these bolometers. There are experimental evidences that the quasiparticle life times in pure Sn is few microseconds or even shorter [82].

The long lifetimes of quasiparticles may arise due to the internal trapping process resulting from internal defects or magnetic impurities, which should also reflect in anomalous heat capacity at low temperature. An extensive review by Phillips [83] gives a compilation of low temperature heat capacity data for metals but the calorimetric data for most of the superconductors exist only above 300 mK, except in few cases like Sn, Al, Re where the heat capacity in the superconducting phase has been measured down to $\sim$150 mK.

Though superconductors like Re, Mo, Zr, Zn, Va, Sn offer similar low heat capacity, only the Sn microcalorimeter has been shown to give an excellent resolution till date [54, 55]. It is important to measure and quantify the heat capacity of Tin absorbers and all other materials used in construction of bolometers (sensor, heater, epoxy) to eliminate the possibility of anomalous heat capacity degrading the resolution of a bolometer. With this motivation the heat capacity of high purity Tin samples has been investigated in the range 60-400 mK.

3.2 Relaxation Calorimetry

Thermal relaxation calorimetric technique [84–87] was used to measure the heat capacity. In this method the specimen is disturbed from its equilibrium temperature (T_0) by supplying a known time dependent input power ($P(t)$) and measuring the temperature response, which is governed by the following relation

$$\frac{d}{dt}\left(\int_{T_0}^{T_0+\Delta T} C(T)\,\mathrm{d}T\right) + \int_{T_0}^{T_0+\Delta T} k(T)\,\mathrm{d}T = P(t) \tag{3.2}$$

where $C(T)$ is the heat capacity of specimen and $k(T)$ is the thermal conductance of the link between the specimen and temperature bath. For small

ΔT, the quantities $C(T)$ and $k(T)$ can be assumed to be constant in the temperature range of T to $T + \Delta T$. The temperature response after turning off the heating power can be approximated as

$$T(t) = T_0 + \Delta T_{max}.\ exp(-t/\tau) \tag{3.3}$$

where ΔT_{max} is the maximum temperature change due to input power and τ is the relaxation time of the system. It can be easily shown that the relaxation time is dependent on the heat capacity of the system and the thermal conductance (k_w) of weak heat link.

$$\tau = C/k_w. \tag{3.4}$$

If the thermal contact between the sample and the platform is poor, the temperature relaxation curve is characterized by a second exponential and is called the 'lumped τ_2 effect' [88, 89]. However, if the thermal conductivity of the sample (k_s) is poor compared to the thermal conductance (k_w) of the weak heat link, the temperature relaxation can be represented by a sum of an infinite series of exponentials. This has been discussed in Refs. [85, 90]. In both these cases the data analysis is complicated as the temperature relaxation deviates from a single exponential.

3.3 Heat Capacity measurement of Copper below 300 mK

Measurement of specific heat of copper has been carried out to qualify the low temperature thermometry, namely, the heater, sensor mounting arrangements and associated electronics. Copper is a well established reference material for evaluating the performance of calorimeters. The specific heat of copper is dominated by the electronic heat capacity ($C = \gamma T$) and the lattice term ($\propto T^3$) can be neglected.

Specific heat of copper was measured using relaxation calorimetry between 100-300 mK. The setup consisted of a thin Cu platform (OFHC copper) supported by teflon posts inside a copper box (Figure 3.1). The teflon posts are the thermal heat links between the copper sample and the thermal bath. A NiCr chip resistor (100 Ω) was used to supply the heat pulse and a commercial Dale ruthenium oxide chip resistor (1 kΩ at room temperature) sensor was used for temperature measurement. The ruthenium oxide chip resistors shows anomalously high heat capacity below 100 mK and hence measurements below 100 mK were not reliable. Both the chip resistors were stuck to the copper platform using GE-varnish. Bare NbTi wires were used for sensor and heater wirings. Current to the heater was supplied by a Keithley 220 programmable current source, while AVS47B AC resistance bridge was used to measure the change in the resistance. The heat capacity for three different masses of OFHC copper (2.620 g , 1.9311 g and 1.4335

Figure 3.1: Setup for measuring the heat capacity of Copper.

g) was measured. There are several reports in the literature of an enhanced specific heat of Cu at low temperatures which have been traced to hydrogen and/or oxygen impurities and lattice defects. Hence, the copper samples (OFHC grade) were annealed at 200^{o}C for 12 hrs prior to measurements, to get rid of any trapped gases. Annealing also removed strains and surface damage from the sample. To extract the specific heat, the difference of heat capacities for two different samples was normalized by the mass difference of the two samples. This ensured that the heat capacity of the addenda and any other systematic error was properly eliminated. The measured value of γ, in the temperature range of 100-300 mK, was 11.1 ± 0.4 μJ/K.g. This is in good agreement with the γ value for copper reported by Martin (10.9 μJ/K.g) [91].

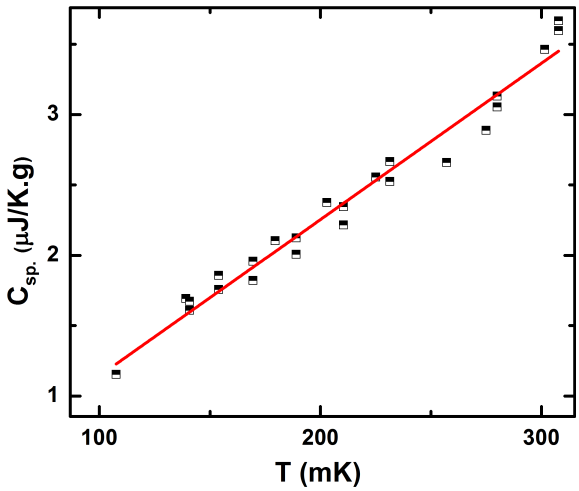

Figure 3.2: The measured specific heat of copper. The symbols denote the data points while the line is the linear least square fitting to the data points.

The specific heat of copper is significantly higher than the specific heat of superconductors below their transition temperature. Therefore, the above setup cannot be used for small sample calorimetry of superconductors like Tin. To measure the heat capacity of Tin, it is necessary to realize an addendum which is as small as possible compared to the heat capacity of the specimen.

3.4 Heat Capacity Setup for Tin

The setup for measuring heat capacity of comprises a sapphire platform (15 mm x 12 mm x 0.4 mm) on which the Tin sample was mounted. The

platform is suspended by insulated NbTi wires (ϕ = 125 μm) inside a Copper box which acts as a thermal bath (Figure 3.3).

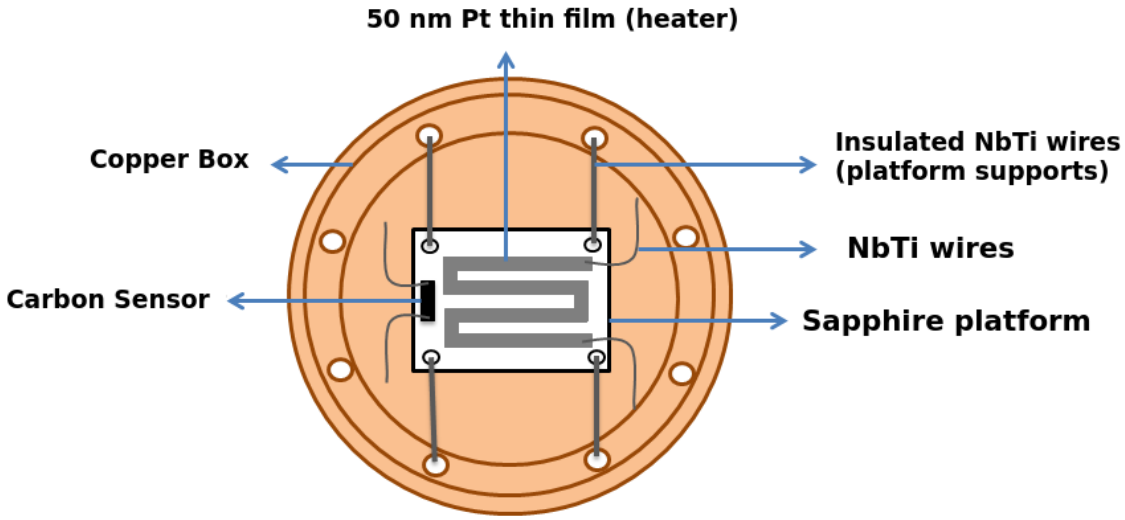

Figure 3.3: Schematic of heat capacity setup for Tin. The NbTi wires along with the platform support wires constitutes weak thermal link to the temperature bath. Superconducting wires are chosen to reduce the contribution of addenda. The sample is mounted on top of the platform sapphire. The Pt heater is on the opposite side.

The weight of the sapphire platform is $\sim$ 300 mg and owing to its very high Debye temperature (1024 K) has negligible contribution to the measured heat capacity at low temperatures. Employing a one dimensional model for the heat flow and assuming that the sample has infinite thermal conductivity when compared to the conductivity of weak thermal links, Bachmann *et. al.* [85] have shown that the about one third of the wire heat capacity should be included as an addendum. Hence, superconducting NbTi

wires were used as weak thermal links for minimizing the electronic heat capacity. The use of other weak thermal links like Constantan, Manganin and Pt-W wires which have anomalous high heat capacity at low temperatures due to presence of magnetic elements in it, was ruled out for these measurements.

Platinum thin film ($t \sim 50$ nm ; $wt \sim 48\mu$g) was deposited on the sapphire platform to obtain a heater with negligible heat capacity (estimated to be $\sim$ 0.16 nJ/K at 100 mK). Platinum was chosen because of its resistance to oxidation and good adhesion to sapphire as compared to Gold. It was verified that the heater resistance ($\sim 550\ \Omega$) was constant in the temperature range of measurements. Thin NbTi ($\sim 80\ \mu$m) wires were bump bonded to Pt heater using Indium dots. The NbTi wires were prepared by etching 125 μm Copper cladded NbTi wire in nitric acid. The ends of the wire were waxed before it was dipped in nitric acid to preserve an extremely small amount of Copper on the ends. This was done as NbTi by itself is not wetted by Indium and the Copper ends facilitate better electrical contact when bump bonded. Also the use of superconducting wires ensured that there is no heat dissipation on the lead wires when the excitation current flows through it.

A Carbon based thermometer has been used as the sensor. The use of Carbon composition resistor from Ohmite Manufacturing Co. for milli-Kelvin thermometry was suggested by Samkharadze *et.al*. [92]. They have shown that this resistor has good thermal contact to its surroundings and can be used down to 5 mK. Following Samkharadze *et.al*., the phenolic package was removed from a 10 Ω resistor and the resistor was thinned down to 0.4 mm. The sensor was stuck to the sapphire platform using a thin layer of fast setting Araldite. Araldite offers better adhesive properties than N-Grease and GE-Varnish, the other two commonly used adhesives at low temperature. Moreover, the thermal conductivity of Araldite is an order of magnitude larger than both N-Grease and GE-varnish. Copper ended NbTi wires were attached to the two ends of thinned Carbon resistor using a small amount of Silver paste. One of the popular alternatives for low temperature sensor is Ruthenium Oxide (RuO_2) based chip resistor. A commercial Dale RuO_2 chip resistor (1 kΩ at room temperature; mass $\sim$ 1.5 mg) was also tried as a sensor. However, it was found out that the heat capacity measured with RuO_2 sensor had a Schottky ($\sim 1/T^2$) contribution at milli-Kelvin temperatures and this significantly overwhelmed the heat capacity of gram sized Tin samples below 150 mK. Similar observations have been reported in the literature [87] and the contribution has been attributed to the magnetic impurities present in the alumina substrate of RuO_2. This

limits the use of RuO_2 chip resistor for heat capacity measurement for small samples of superconductors below 150 mK. As will be shown later, no such Schottky contribution is observed for the Carbon sensor used in our setup.

The measurements were carried out in a high cooling power (1.4 mW at 120 mK) cryogen-free dilution refrigerator setup at TIFR, Mumbai [93] described in the previous chapter. The whole setup is enclosed within a Faraday cage for EMI shielding. The dilution unit has an additional option of top loading probe insert which gets connected to mixing chamber and facilitates easy sample changes in cold condition. The heat capacity setup was attached to the probe insert. The Carbon sensor was calibrated against a secondary resistance thermometer (S1109) attached to the mixing chamber of the dilution refrigerator.

The heater current was supplied by a Keithley 220 programmable current source. The DC supply voltage lines were filtered using a 3-stage RC filter (located at room temperature) with 30 ms time constant to suppress the high frequency noise emanating from the current source unit that could heat up the platform. This filter time constant ($\sim$ ms) is much smaller than the measured time constant ($\sim$ few secs) and hence did not affect the heat capacity measurement. An AVS 47B AC resistance bridge was used to measure the change in the resistance with a sampling rate of 1.5 samples/sec. To prevent self heating of the sensor a low excitation voltage was used such that the

power dissipated in the sensor was less than 1 pW. The heater power was chosen such that the ΔT was within 5% of the base temperature T_0. The base temperature T_0 was independently controlled and multiple measurements of temperature decay curve were made at each base temperature (Figure 3.4). The decays were single exponential and no 'lumped τ_2 effect'was visible

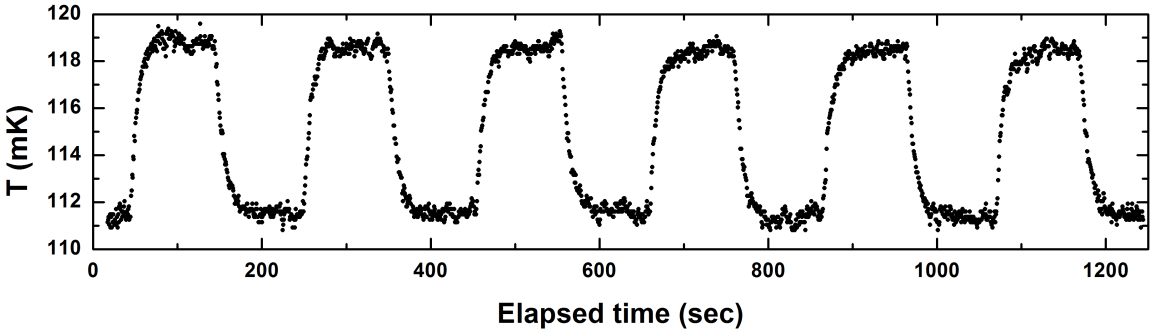

Figure 3.4: A typical picture of the measured temperature variation of the Carbon sensor in response to a square-wave current supplied to the heater on the sapphire platform (see text for details). Each of the thermal relaxation curve is fitted to a single exponential to obtain a time constant. The relaxation time constant τ is obtained by doing a weighted average of time constants of all curves.

(Figure 3.5).

The data was also analyzed using dual slope method [94] and no difference was found as compared to the method of fitting the temperature decay with a simple exponential curve. The sensor saturated below 60 mK indicating that the thermal contact of the platform to the cold bath is extremely weak and platform is unable to cool down in the presence of background heating. The background heating could be due to the hanging arrangement

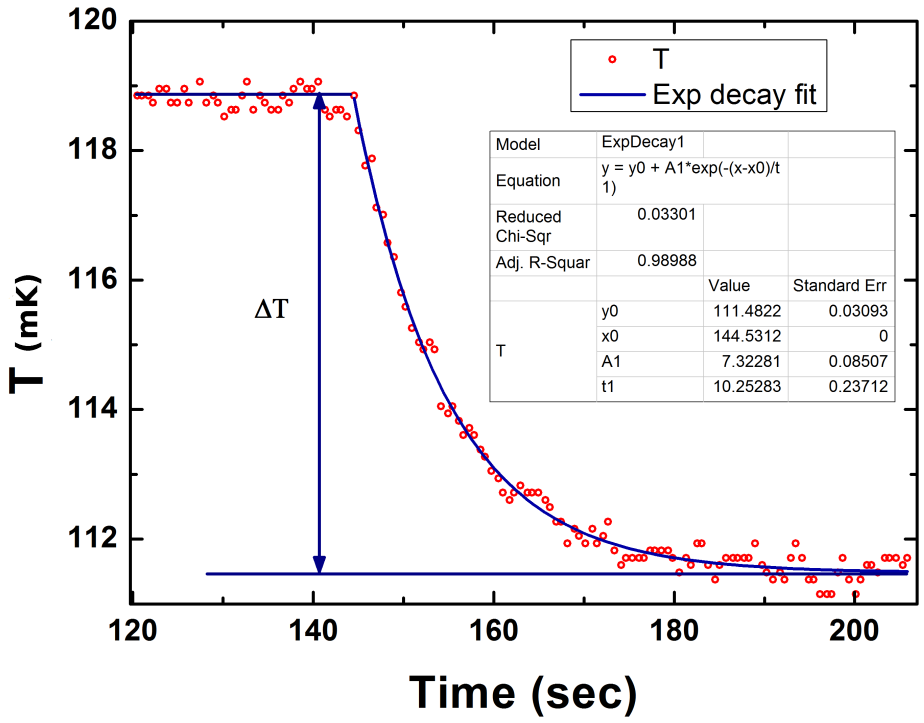

Figure 3.5: A typical relaxation pulse fitted with exponential decay function.

of the platform, which can capture the vibrations of the probe insert of the dilution refrigerator on which it is mounted. Johnson noise from higher stages of the dilution refrigerator radiated down the electrical lines of the thermometer and heater can be another reason for overheating. The heat capacity setup is mounted inside a copper box which is closed from all sides except for few holes for electrical connection and evacuation. The copper box and a thermal shield at the 50 mK stage of the dilution refrigerator ensure that the radiation heat load from higher stages of dilution refrigerator is minimized.

To get the specific heat of Tin, heat capacity of two different masses ($M_1 = 3.0826$ g and $M_2 = 2.5819$ g) of high purity (99.999%) Tin were measured. The samples were stuck on the sapphire platform using a thin layer of Apiezon N-grease. The difference between the two measured heat capacities, normalized by the mass difference, eliminates all systematic errors and contribution from the addenda. The subtraction method does not completely eliminate the heat capacity contribution from the N-grease which was used to stick the sample on the platform. Since, only a thin layer of N-grease was applied it is difficult to exactly quantify its amount. However, since both the samples have similar surface area, it was assumed that the amount of N-grease used in both the cases would be nearly equal.

3.4.1 Thermal Conductance of NbTi wires (k_w)

It is important to accurately measure the thermal conductance of the weak heat link to the cold bath as it changes appreciably with temperature. The thermal conductance is calculated from the applied power P and measured ΔT according to the relation

$$k_w = \frac{P}{\Delta T} \tag{3.5}$$

It can easily be shown that for small ΔT, the criteria, $k_w(T) = k_w(\bar{T})$ and $C(T + \Delta T) = C(\bar{T})$, are satisfied for the above relation to hold good. Figure 3.6 shows the measured conductance of the weak heat link for both the Tin samples. The measured conductance can be approximated to the power law $k = a\,T^b$ and the fit values obtained are

$$k_w(T) = 0.32\,T^{2.06}\,\mu W/K \tag{3.6}$$

From this fit, the absolute thermal conductivity of NbTi wire is estimated and is shown in the inset of Figure 3.6. Here it is assumed that the NbTi wires provide parallel paths for the heat leak to the thermal bath for the arrangement given in Figure 3.3. The systematic error in thermal conductivity due to uncertainties in length estimation of NbTi wirings for the sensor and the heater is less than 10%. The lattice conductivity of polycrystalline NbTi deviates from the Debye model at low temperatures where $k \propto T^3$ dependence is expected. The measured T^2 dependence can be better understood in the framework of 'glass-like' lattice vibrations in NbTi at low temperatures [95] and is consistent with the thermal conductivity of NbTi wires as measured by Olson [96]. Therefore, in the present case the main contribution to the thermal conductance is only due to the NbTi wires. The measured thermal conductance to the bath and the fact that only a single

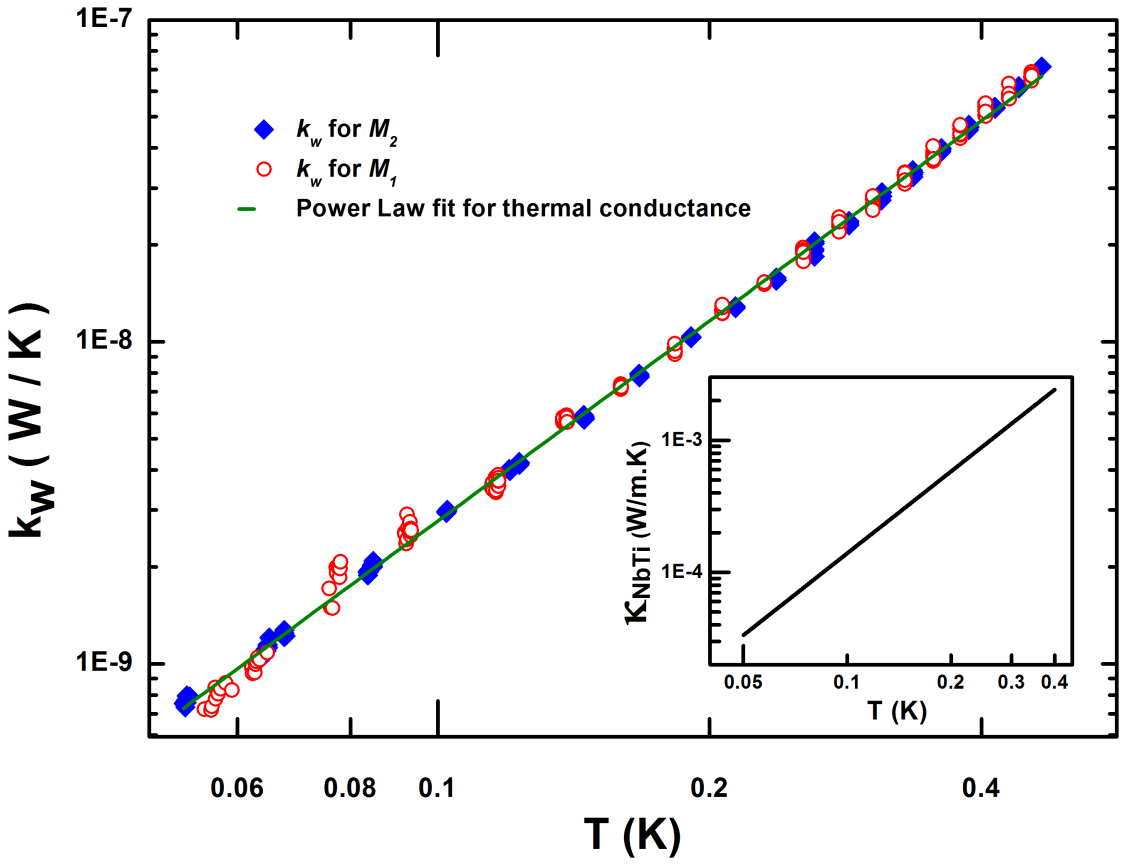

Figure 3.6: The measured thermal conductance of the weak heat link for different measurement runs and its power law ($k = a\,T^b$) fit. Estimated thermal conductivity of NbTi wire is also shown in the inset (see text for details).

exponential decay time constant was observed implies that the thermal conductance between sample and the platform is much larger than the k_w. The thermal conductance also serves as a diagnostic measure to ensure that the mounting arrangement is identical for different runs.

3.4.2 Specific Heat of Tin

The Tin sample plus platform was heated to an equilibration temperature ΔT above a constant reference temperature T_0 and then the heater was turned off. The temperature decay was fitted to a single exponential to obtain time constant. The masses have been chosen to ensure that the τ is of the order of 5-15 secs in the temperature range of measurement. The heat capacity of the sample was extracted using Eq. (3.3) and Eq. (3.4). Heat capacity data for both the samples are shown in Figure 3.7 and Figure 3.8, where the ratio of C/T is plotted against T^2.

The straight line fit to the data shows that the measured heat capacity has only linear and cubic dependences on the absolute temperature. There is no Schottky like term ($\sim T^{-2}$), which suggests the absence of any magnetic impurity in the sample and the constituents of the platform. The heat capacity values obtained from the fit are

$$C_{M_1} + C_{addenda} = (210 \pm 5)T + (9502 \pm 128)T^3 \; nJ/K \qquad (3.7)$$

$$C_{M_2} + C_{addenda} = (209 \pm 3)T + (8464 \pm 69)T^3 \; nJ/K \qquad (3.8)$$

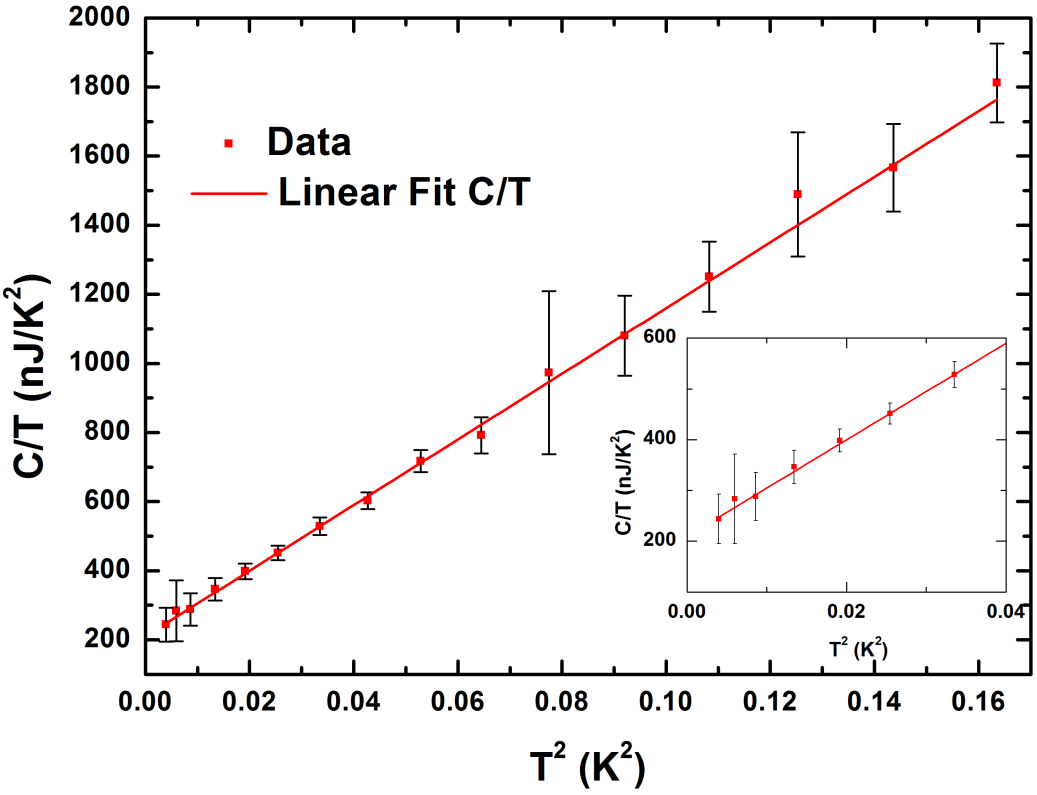

Figure 3.7: The measured heat capacity of M_1 together with addenda. The error bars are due to the standard deviation of the measured time constants (τ) for multiple heat pulses at same base temperature. The inset shows the data from 60-225 mK.

The linear term dominates at low temperature and limits the sensitivity of the setup to measure heat capacity at lower temperatures. The constancy of its coefficient in both Eq. (3.7) and Eq. (3.8) indicates that the contribution to the linear term is from the platform and not from the sample. By subtracting (3.8) from (3.7) one gets

$$C_{M_1-M_2} = (1038 \pm 145)T^3 \; nJ/K \tag{3.9}$$

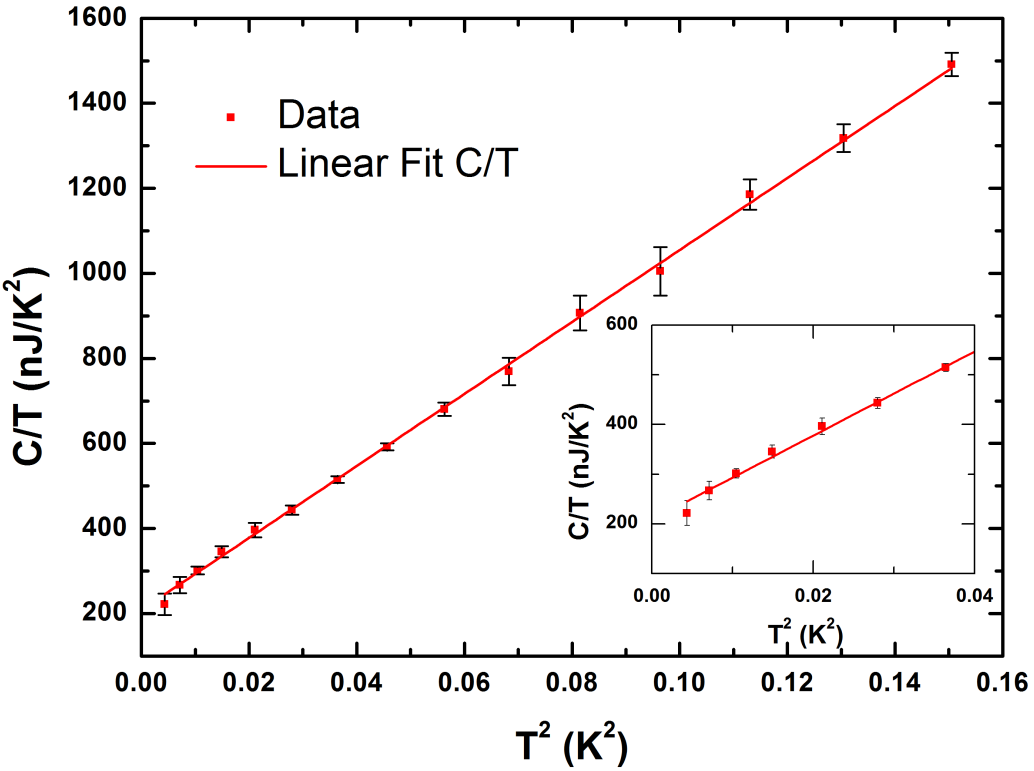

Figure 3.8: Same as in Figure 3.7 but for M_2 together with addenda.

When normalized to the mass difference the specific heat of superconducting Tin is obtained as $(2073 \pm 290)T^3\ nJ/K.g$, which gives the value of Θ_D as (199±9) K. This is consistent with the reported values on Tin obtained by calorimetric measurements at higher temperatures by O'Neal & Phillips [97] (Θ_D = 198 K) and Bryant & Keesom [98] (Θ_D = 200 K). This is also in good agreement with the Debye temperature obtained from measurements of the elastic constants of Tin (Θ_D^{el} = 201 K) [99].

3.4.3 Comparison of Polycrystalline Tin vs Single Crystal

Most of the superconducting Tin microcalorimeters absorbers reported in literature are polycrystalline in nature. In a polycrystalline superconductor absorber, the quasiparticles can scatter at the grain boundaries and can transfer its energy to the lattice system, thereby achieving better thermalization. To investigate if this leads to differences in the heat capacity, measurements on polycrystalline and single crystal Tin were done and compared. The heat capacity of three different masses of 5N purity Tin (2.8448g

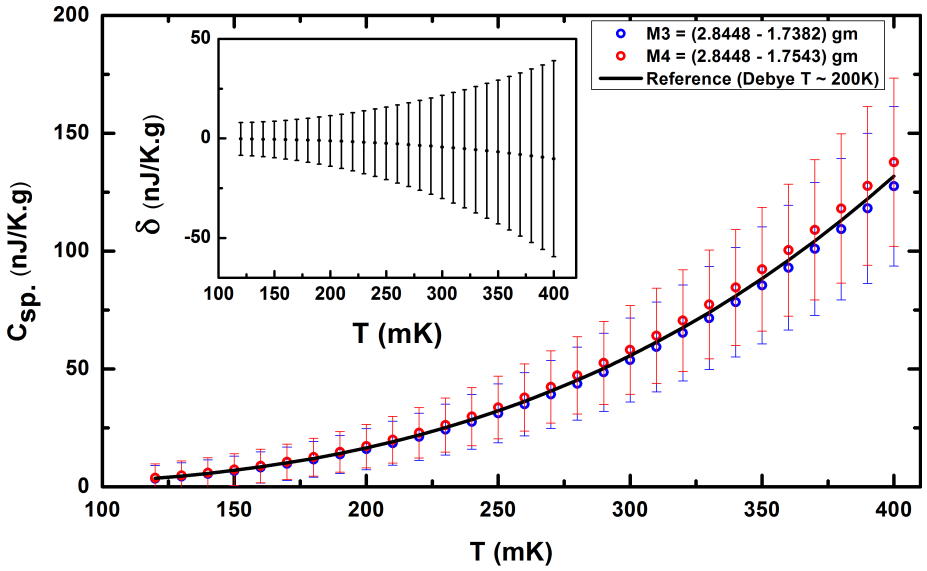

Figure 3.9: Measured specific heat for polycrystal and singe crystal Tin. Three different masses of 5N purity Tin (2.8448g - polycrystalline, 1.7543 g -polycrystalline and 1.7382 g - single crystal) were measured along with the addenda. Data using Debye temperature is also shown for comparison. The inset shows the difference of the measured specific heat for the samples ($\delta = C_{M3} - C_{M4}$) along with the errors for better visibility.

- polycrystalline, 1.7543 g -polycrystalline and 1.7382 g - single crystal) were measured along with the addenda. To extract the specific heat, the difference of heat capacities for two different samples was normalized by the mass difference of the two samples. It can be seen from the Figure 3.9 that within measurement errors no difference is found between the heat capacity of a polycrystal and a single crystal sample at low temperatures.

3.5 Summary

The calorimetry technique was qualified by measuring the heat capacity of copper in the temperature region of interest. A calorimeter set up has been devised to measure ultra small heat capacity of superconductors below 400 mK using Carbon sensors made from commercially available Carbon resistors. The setup is inexpensive and uses off the shelf low temperature electronics to measure the heat capacity. Specific heat of Tin has been measured on the setup in the range of 60-400 mK and has been found to be in good agreement with the earlier reported values of Tin which corresponds to a Debye temperature of Θ_D = 200 K. Measurement below 60 mK were limited due to the thermal decoupling of the sapphire platform from the temperature bath in presence of background heating (vibrational noise) and not due to the the cooling of the mixing chamber of the dilution refrigerator.

The absence of anomalous heat capacity in the Tin sample at ultra low temperature along with the result of quasiparticle lifetime saturation by Visser *et.al*. suggests that it should be possible to achieve complete thermalization of energy in a Tin bolometer absorber. Also, no difference is found between the heat capacity of a polycrystal and a single crystal sample.

Chapter 4

Simulation studies for the Tin Bolometer array

4.1 Introduction

As explained in Chapter 1, the sensitivity of a $0\nu\beta\beta$ experiment critically depends on the active mass of the detector, the background level and the resolution of the detector. Since the sensitivity for half-life measurement increases with mass (linearly for zero background, realistically as $\sqrt{M}$), increasing the mass of the detector is the easiest way of improving the sensitivity. The TIN.TIN will employ a modular structure wherein a closed packed array of detector modules will be operated at cryogenic temperature. Each module itself will consist of several detector elements. For macro-bolometers, a tower geometry is preferred owing to the ease of operations for assembly of the detector modules and associated thermometry.

This also facilitates easy upscaling to larger sizes. In addition, the granularity of the detection volume can also be used for the identification of physics processes, which may help in discrimination of the background events. The structure of the array and the size of the individual detector element needs to be designed based on

- Calorimetry requirements.
- Effectiveness of detector granularity to discriminate multi-site events from double beta decay events (which originate at a single site).
- Constraints on the number of sensors, associated wirings and readout electronics.

Monte Carlo simulations for optimizing the design of a Tin detector module has been performed by varying element sizes and geometries, with an emphasis on the background reduction capabilities of the module.

4.2 Optimization of the element size for calorimetry

It is straightforward to see that larger is the mass of the detector, higher is the probability to detect a $0\nu\beta\beta$ event. A large scale experiment (10 - 1000 Kgs) would necessarily require an array of smaller detector modules. It is desirable to have a fewer number individual detector elements in the module, in order to restrict the number of readout channels and to reduce

the dead volume. However, the mass of a single detector element has a limitation since the heat capacity increases linearly with the mass. Consequently, the temperature increase corresponding to a given deposited energy (pulse height), diminishes with increasing mass of the detector element. The size of an individual bolometer detector element needs to be optimized for a measurable temperature rise (ΔT) per unit energy of the absorbed radiation. The design goal for the TIN.TIN is to achieve a ΔT of $\sim 100\mu$K for a thermal pulse corresponding to E $\sim$ 2 MeV deposited in the element (similar to CUORE [36] detector), at base temperature ranging from 10-30 mK. A smaller ΔT may be affected by a poorer signal to noise ratio, which will subsequently degrade the desired resolution of the detector. For a Tin detector element of mass m, the temperature rise ΔT ($\ll T$) can be written as,

$$\Delta T = \frac{E}{m.C(T)} = \frac{E}{(\rho V)(\beta T^3)} \tag{4.1}$$

where ρ and V are the density and the volume of the Tin detector element, respectively. At T = 10-30 mK, the heat capacity of Tin is assumed to be only due to the lattice contribution ($C(T) = \beta T^3$). It is easy to see from Eqn. 4.1 that the maximum permissible volume V of the detector element varies as $1/T^3$ for a fixed ΔT. This is also shown in Figure 4.1, where the maximum permissible volume of the Tin detector element is plotted as a function of the base temperature for the desired ΔT $\sim 100\mu$K at E$\sim$ 2 MeV.

It can be seen that at ∼10 mK, the maximum volume of the Tin detector

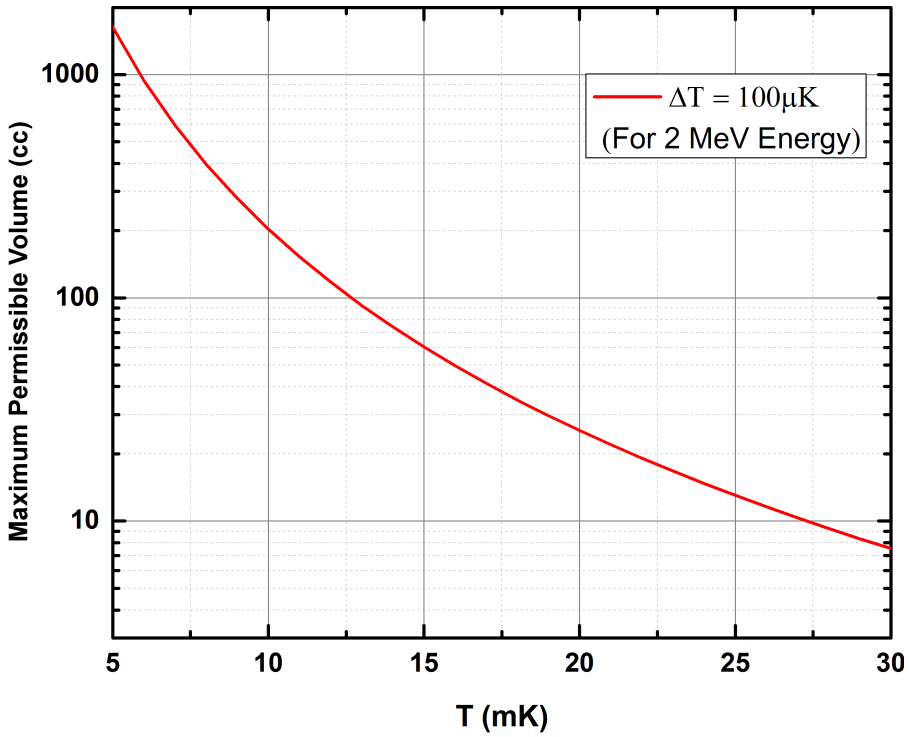

Figure 4.1: Maximum permissible volume of a Tin detector element as a function of base temperature for the desired $\Delta T \sim 100\mu K$ at E∼ 2 MeV.

element for which an appreciable pulse height can be obtained is ∼ 200 cm^3. A smaller element size would be desirable for a larger pulse height at the lowest base temperature.

4.3 Optimization of the element size for the background reduction

The sensitivity of the detector is also critically dependent on the reduction of background. The cosmogenic background is significantly reduced in underground laboratories, but background contribution from the decay of the radioactive trace impurities present in the detector (α, β and γ) and in the surrounding materials cannot be completely eliminated. It is important to discriminate this background from the $0\nu\beta\beta$ events of interest. The experimental signature of $0\nu\beta\beta$ decay consists of measuring the sum of the kinetic energies of the electrons, which is equal to the Q value of the double beta decay ($Q_{\beta\beta}$). Emitted electrons will dominantly deposit their energy in the Tin detector element by ionization. The size of the individual element should be chosen such that the detector dimensions are large compared to the range of the electrons, thereby increasing the probability to contain the $0\nu\beta\beta$ events within the element. Typical range of 2 MeV electrons is of the order of few millimeters, and hence $0\nu\beta\beta$ events can be contained within a small volume of the detector element. Therefore, the size of the individual detector element can range from a few cc to hundreds of cc. Moreover, it is desirable to have a smaller surface-to-volume ratio as it reduces the background per unit mass originating from the surface background [100].

All radioactive materials with Q values greater than $Q_{\beta\beta}$ are potential background sources for the $0\nu\beta\beta$ decay. A fraction of the energy close to $Q_{\beta\beta}$ released during the decay can be deposited in the detector. Surface contamination with ^{210}Pb or other isotopes which decay via α emission ($E_\alpha = 2 - 10$ MeV) can be a significant source of the background. However, if the detector element is of high radiopurity then the background will be dominated the gamma-rays from the surrounding. Gamma-rays, resulting from natural decay chain or neutron induced reactions, have energies varying from 100 keV to 10 MeV. Photons from the decays of ^{208}Tl, ^{214}Bi (end products of natural radioactive decay chains) etc., dominate the background in the region of interest. In this energy range, the gamma-rays predominantly interact via Compton scattering. The absorption length of these high energy photons in Tin is of the order of centimeters. Unlike electrons, photons would typically interact with more than one detector element and can deposit only a fraction of the total energy in a single element detector. It is therefore possible to use the hit multiplicity (M) to discriminate between electrons and gamma-rays in a limited manner. If the multiplicity of an event is denoted by M, then total photon events detected in the module can be written as

$$N_{total} = (N^p + N^c)_{M=1} + (N^p + N^c)_{M>1} \tag{4.2}$$

where N^p and N^c are the photopeak and the Compton scattered events, respectively. The $M > 1$ events are expected to predominantly arise from photons and can be rejected during analysis with the multiplicity condition. Photons with $M = 1$ can be clearly identified if it is a photopeak event ($N^p_{M=1}$). Difficulty arises for identification and rejection of Compton scattered $M = 1$ photon events ($N^c_{M=1}$). It is thus essential to choose an array configuration where the $N^c_{M=1}$ is minimized. Since the energy resolution of the bolometer is expected to be better than 10 keV, the background in the region of interest for $0\nu\beta\beta$ decay mainly arises from the Compton scattering of higher energy ($> Q_{\beta\beta}$) gamma-rays.

Simulations have been carried out to study the background resulting from gamma-ray interactions for different element configurations to optimize the size of the detector element and the module. The GEANT4 [101] package was used for the simulation of particle tracking, geometries and physics processes. Photons of a given energy were randomly generated on a spherical surface enclosing a 3D array of cubic Tin detector elements of different sizes. Details of the module geometry are given in Table. 4.1 and shown schematically in Figure 4.2. In each case the total volume of the module is kept the same. A gap of 5 mm was kept between the individual elements in all the simulations, though the choice of the gap size would depend upon the support structure of the individual elements. The fluence in each direction

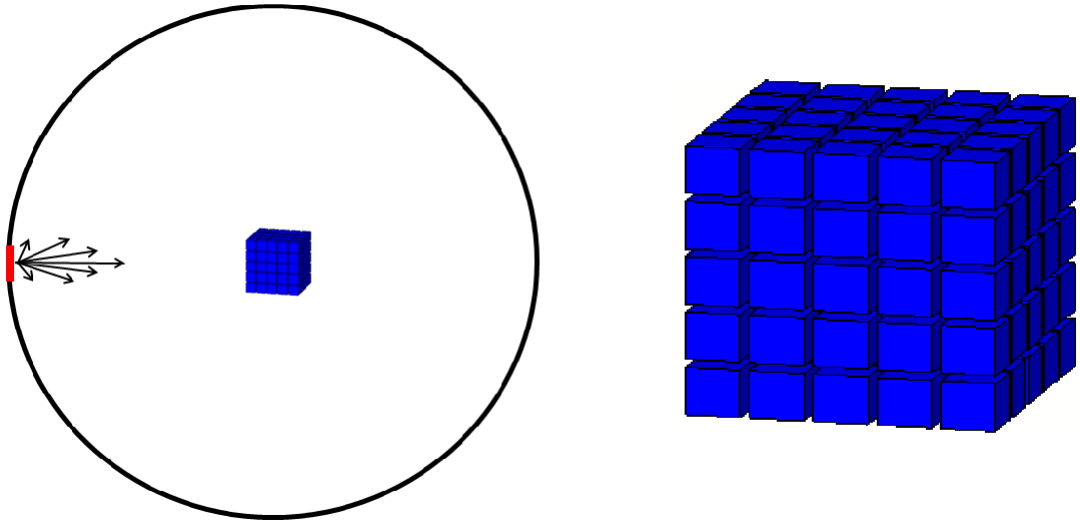

Figure 4.2: A pictorial view of the spherical surface source enclosing a 3D array of cubic Tin detector elements (left). A typical geometry of the element array used in simulation (right). The radius of the source sphere is much larger than the module size.

was kept proportional to the cosine of the angle between source direction and the local normal to the sphere surface. The radius of the sphere was kept much larger than the element size to ensure uniform illumination of the entire module. The detector multiplicity was defined as the number of elements in an event where the deposited energy is larger than the preset threshold of 10 keV. Photon energies considered cover the range of interest

Table 4.1: Detector module configuration used in simulations

Individual element size (cc)	Total number of elements	Total Volume (cc)
2.143 x 2.143 x 2.143	7 x 7 x 7 = 343	3375.6
3 x 3 x 3	5 x 5 x 5 = 125	3375
5 x 5 x 5	3 x 3 x 3 = 27	3375

for natural background radiations. The most prominent gamma radiations are from the ^{238}U and ^{232}Th series and ^{40}K decay, with the maximum energy of 2615 keV from the ^{208}Tl decay. Higher energy gamma-rays also exist, for example the 3183 keV from ^{214}Bi, but the branching ratio is negligible (0.00133%). Sufficiently large number of events (10^7) were generated to minimize the statistical fluctuations in the simulated data.

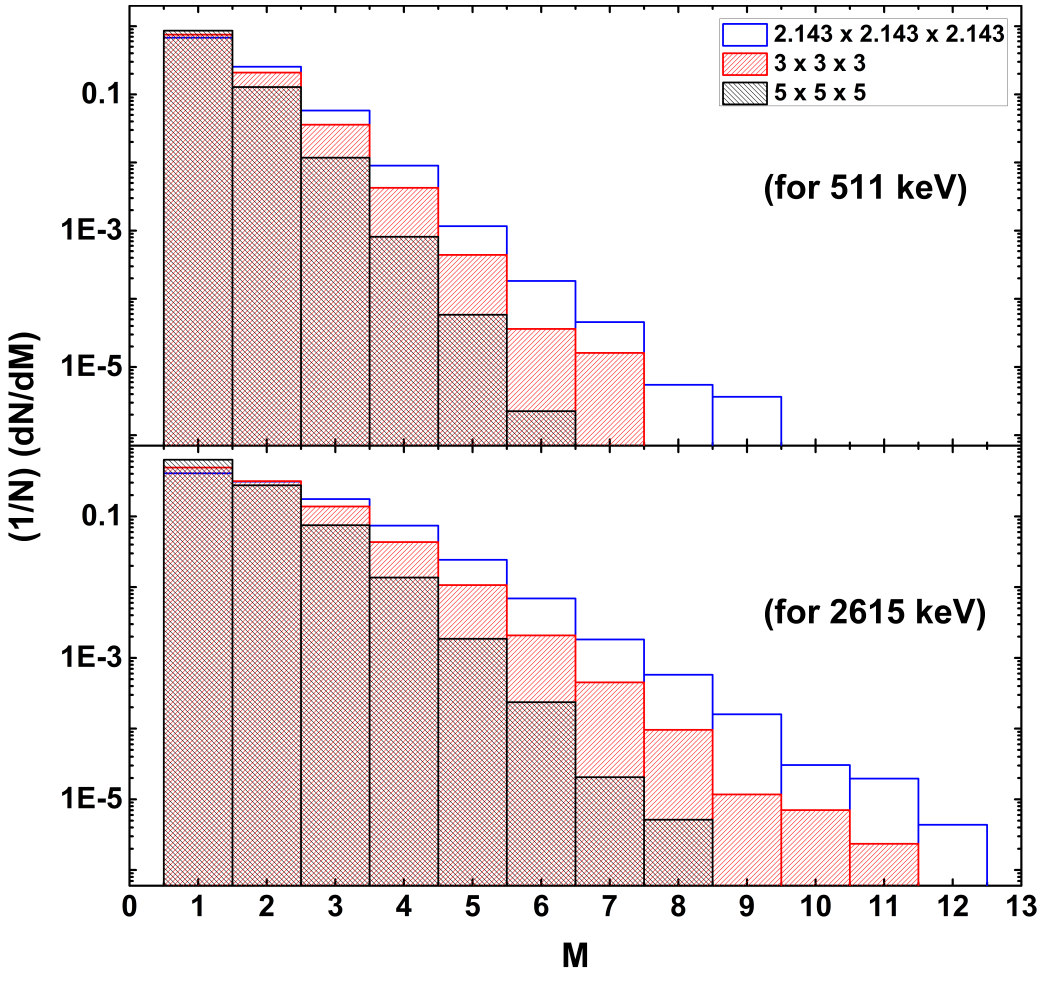

Figure 4.3: Simulated Multiplicity distribution for E_γ= 511 keV and 2615 keV for different element sizes.

The multiplicity distribution of the detector for 511 keV and 2615 keV is shown for different configurations in Figure 4.3. The multiplicity distribution is narrower for larger element size and lower photon energy. Table 4.2 shows the average multiplicity for 511 and 2615 keV for different element sizes.

Table 4.2: Average multiplicity ($< M >$) and standard deviation ($\sigma_{<M>}$) for 511 keV and 2615 keV for different element sizes.

Energy (keV)	Element size (cm)	$< M >$	$\sigma_{<M>}$
511	2.143	1.4	2.3
511	3	1.3	2.0
511	5	1.2	2.0
2615	2.143	2.0	2.8
2615	3	1.8	2.6
2615	5	1.5	2.1

Figure 4.4 shows the probability for discrimination of a photon based on a multiplicity condition of $M > 1$. It is evident that smaller the size of an individual element, greater is the probability of discrimination of $M > 1$ events. The background rejection ratio, defined as $N_{M>1}/N_{total}$, at 2615 keV is only $\sim$5% worse for a=3 cm as compared to that for a= 2.143 cm, while it is about 2/3rd for a=5 cm. Figure 4.5 shows the fraction of Compton scattered events with $M = 1$. It can be seen that detector elements with a= 2.143 cm and a= 3 cm show very similar behaviour, while a=5 cm is worse

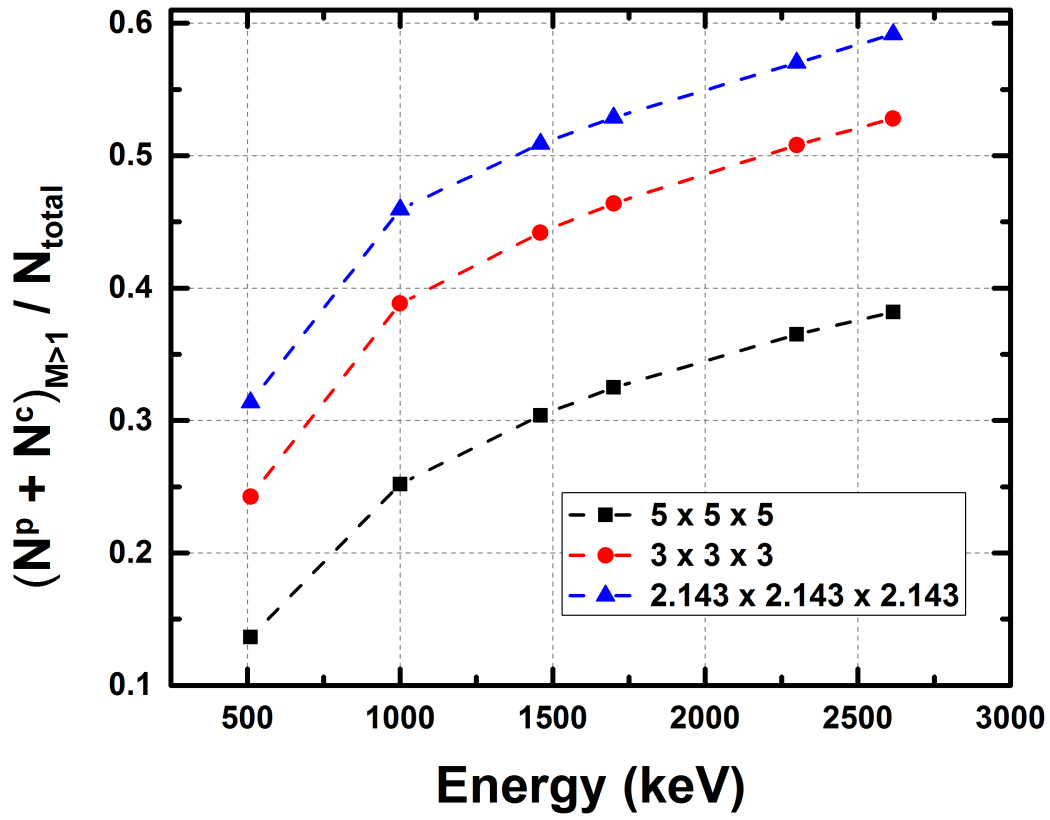

Figure 4.4: The probability of $M > 1$ events as a function of photon energy for different element sizes (see text for details). Lines are only to guide the eye.

by about 20%. It can be seen that the $N^c_{M=1}$ for a= 2.143 cm is greater than that for a = 3 cm and 5 cm at lower energies whereas, at higher energies ($\geq$ 1500 keV) the $N^c_{M=1}$ for a= 2.143 cm is smaller than that for a = 3 cm and 5 cm elements. This can be understood considering the half thickness ($d_{1/2}$) for the absorption of photons in Tin compared to the element size. For $E_\gamma \geq$ 1500 keV, the $d_{1/2}$ for Tin is more than 2 cm [102]. Therefore, at higher energies the probability for multiple hits ($M > 1$) increases for

smaller crystal sizes, which is reflected in Figure 4.5 as the reduction of $N^c_{M=1}$ events.

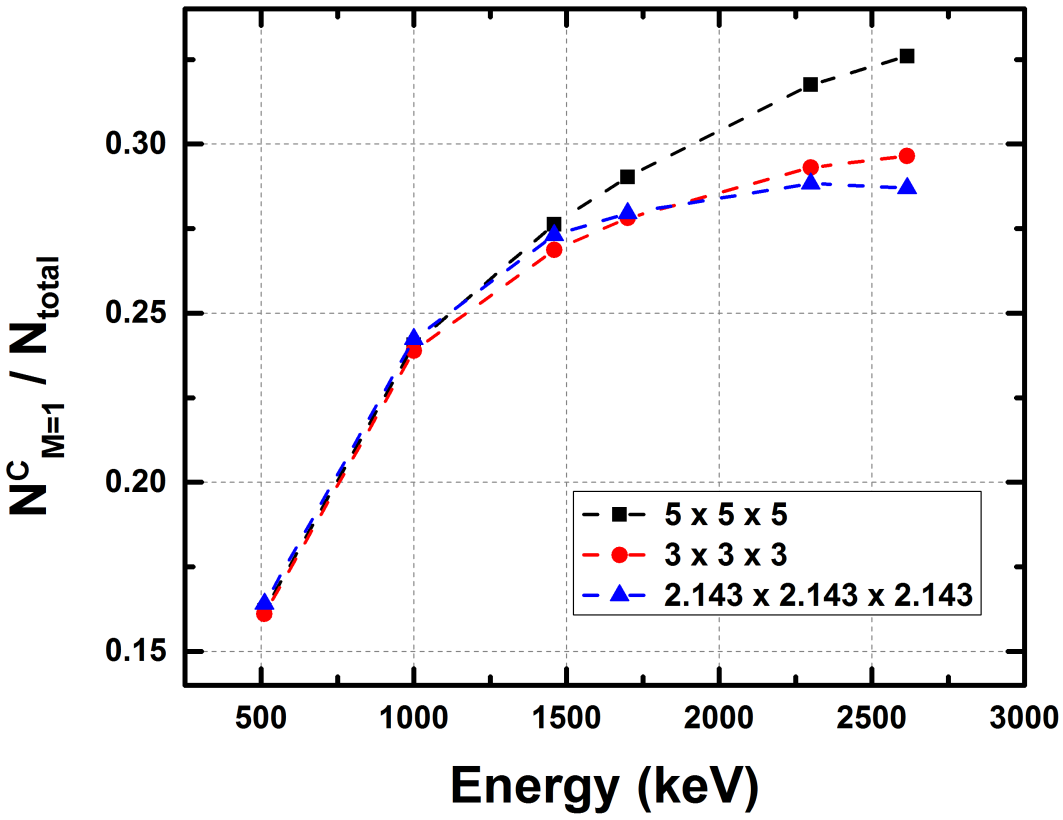

Figure 4.5: The probability of $N^c_{M=1}$ events as a function of photon energy for different element sizes (see text for details). Lines are only to guide the eye.

The effect of inter detector spacing was also studied by varying the gap from 2 mm to 10 mm. A larger gap between the detector will increase the probability of gamma-rays escaping after Compton scattering. This will increase the $N^c_{M=1}$ events, thereby increasing the background with inter detector spacing. Therefore, a minimum inter detector spacing is preferable.

It should be noted that decreasing the detector element size results in increased number of readout channels. For the same total mass of $\sim$25 kgs, a Tin detector module with a = 2.143 cm (343 elements) will require $\sim$ 3 times more number of sensor readouts than that for a = 3 cm (125 elements). A detector array with very larger granularity (like 343 elements) would require an upscaling of wirings inside the cryostat, cold electronics (if the preamplifier stage is located at the 50 K station for better noise immunity) and data acquisition electronics at room temperature. Also, an increased number of sensors would correspond to more surrounding material (connecting wires etc.) which will contribute the background, thereby adversely affecting the sensitivity. From the Figure 4.4 it can deduced that the multiplicity discrimination for a = 2.143 cm at 2615 keV is only $\sim$5% better than that for a = 3 cm. Thus, it appears that 3 x 3 x 3 cm^3 element size provides the optimal granularity for the background discrimination of the gamma events and the number of readout channels.

It is envisaged that the prototype of the TIN.TIN detector will consist of elements of sizes 3x3x3 cm^3 with corresponding readout sensors. Each module will consist of 27 elements ($\sim$5 Kg), arranged in a cubic array of 3 x 3 x 3 such that the central element is covered on all sides by other detector elements. The modules can be arranged in a tower geometry for upscaling to large mass experiments in a phased manner.

4.4 Intrinsic efficiency of a detector array for $0\nu\beta\beta$ decay

A calorimeter can have very high detection efficiency for $0\nu\beta\beta$ decay events. The energy equal to $Q_{\beta\beta}$ (2292 keV for ^{124}Sn) of the decay is shared between the two emitted electrons. As mentioned earlier the range of 2 MeV electrons in Tin is $\sim$ 2 mm, almost all the events are contained inside the detector except for the surface events. There are two possibilities for the $0\nu\beta\beta$ surface events (Figure 4.6)

- Partial energy is deposited in one element while the rest escapes detection. These events cannot be reconstructed back and determine the absolute intrinsic efficiency of an detector array.

- Partial energy is deposited in neighbouring detectors. In this case the events can be reconstructed by demanding a time coincidence between two adjacent elements.

Simulations were done to determine the intrinsic efficiency of a detector module consisting of 27 cubic elements of the optimized size of 3x3x3 cm^3. A fortran based code, DECAY0 [103] was used as a event generator for $0\nu\beta\beta$ for ^{124}Sn. The program generates the initial energy, time and angular distribution of the electrons emitted during the decay process. The events were generated randomly inside the active volume of the detector module.

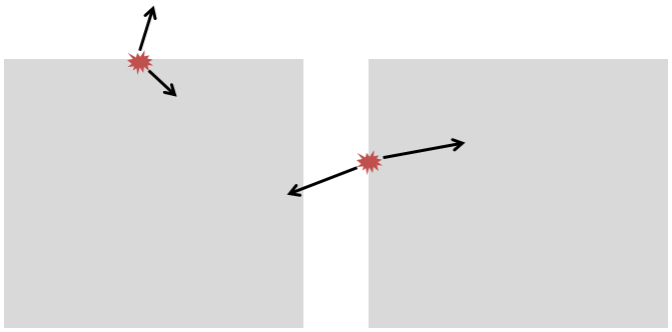

Figure 4.6: A schematic picture for a surface event for $0\nu\beta\beta$ decay. The decay occurs near the surface of one of the detectors depositing the energy into it. The escaping radiation can either be detected by a neighbouring detector element or can escape detection.

The particle interaction in the detector element was simulated and propagated using the GEANT4 package. Sufficiently large number of $0\nu\beta\beta$ events (10^5) were generated to minimize the statistical fluctuations of the simulation data. The default low energy cut-off in GEANT4 was 1 keV. However, a hit was defined if the energy deposited inside a crystal was more than 10 keV. Figure 4.7 shows the energy response of the entire module (27 elements). The total efficiency of the detector array is about $\sim 93\%$ for all multiplicities ($M \geq 1$). The rest 7% of the events deposit only partial energy in the detector module. Events with $M > 1$ can be rejected in order to effectively reduce the background contribution in the region of interest. In this case the net intrinsic efficiency of the detector module decreases to 86% as shown in the inset of the Figure 4.7. The loss of 14% efficiency is consistent with the ratio of surface-to-volume events for a 3x3x3 cm^3 element size. It

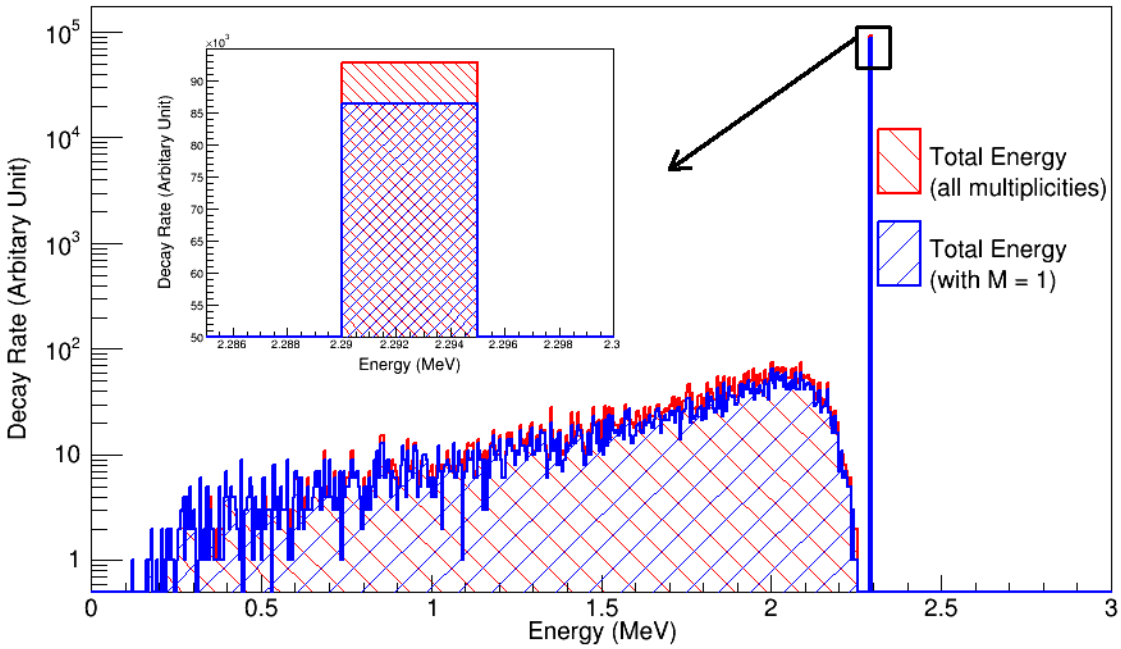

Figure 4.7: Simulated energy spectrum (5 keV/bin) for $0\nu\beta\beta$ in the detector module consisting of a cubic array of 27 elements. The efficiency of the array to detect $0\nu\beta\beta$ events at the Q value is about 93% and 86% for ($M \geq 1$) and ($M = 1$), respectively.

should be noted that the resolution of the detector has not been folded in for the histograms.

4.5 $2\nu\beta\beta$ background to $0\nu\beta\beta$ events

Another source of background in the region of interest near $Q_{\beta\beta}$ is due to the $2\nu\beta\beta$ decay events. In the $2\nu\beta\beta$ decay process the result is a continuum beta-like spectrum for the energy deposited by the electrons. If the

energy resolution of the detector is poor, then it will be difficult to distinguish the $0\nu\beta\beta$ energy peak at the endpoint from the $2\nu\beta\beta$ background. In case of calorimetric detectors, which have excellent energy resolution, the background from $2\nu\beta\beta$ decay to the $0\nu\beta\beta$ is expected to be small.

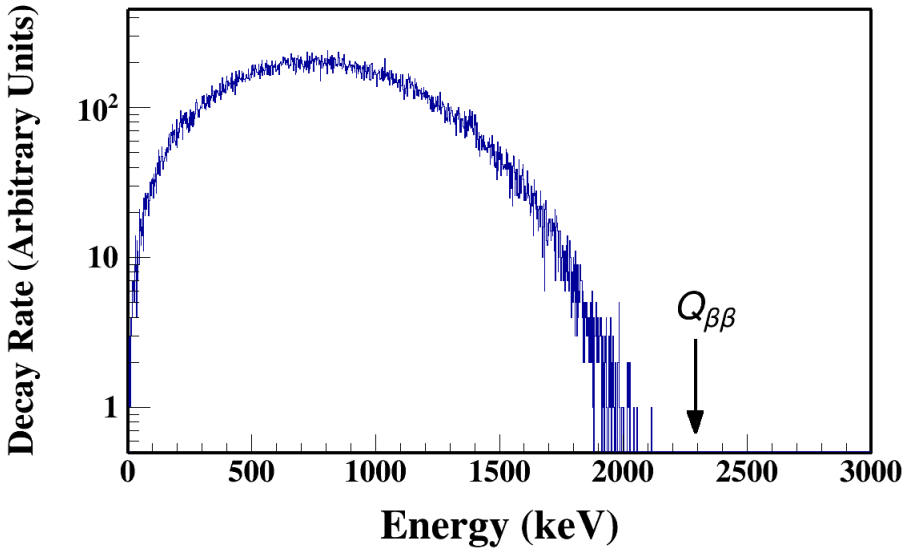

Figure 4.8: Simulated energy spectrum for $2\nu\beta\beta$ in a cubic 3x3x3 element array. For expected resolution of $\sim$ 5 keV at 2292 keV, the estimated background contribution to the energy region of interest is negligible.

The sum electron spectrum for $2\nu\beta\beta$ is of the form [104]

$$\frac{dN}{dK} \sim K.(Q_{\beta\beta} - K)^5.\left(1 + 2K + \frac{4K^2}{3} + \frac{K^3}{3} + \frac{K^4}{30}\right) \qquad (4.3)$$

where K is the sum of the kinetic energies of both electrons. Assuming the region of interest for $0\nu\beta\beta$ to be (2268 keV - 2293 keV), the fraction

of $2\nu\beta\beta$ events in the region of interest is estimated to be $\sim 10^{-9}$. The region of interest has been defined as the 5σ energy window near $Q_{\beta\beta}$, with an expected energy resolution of 10 keV (FWHM). According to the theoretical predictions the decay rate of $0\nu\beta\beta$ and $2\nu\beta\beta$ in ^{124}Sn is $\sim 10^{26}$ yrs and 10^{20} yrs, respectively [105]. Hence, the background contribution due to $2\nu\beta\beta$ in the region of $0\nu\beta\beta$ is estimated to be less than 0.1% for a cryogenic Tin bolometer detector.

4.6 Summary

Simulations have been carried out to optimize the detector element size for photon background reduction based on hit multiplicity. The present studies indicate that a 3x3x3 cm^3 element for a detector module would be a suitable choice for calorimetry, background discrimination of gamma events and the number of readout channels. The optimized module is a cubic array of 27 elements arranged in a 3x3x3 geometry. The expected efficiency for this module is $\sim$ 86% for $0\nu\beta\beta$ events. By using the multiplicity information from the segmented array, gamma-ray background reduction can be improved.

Chapter 5

Summary and Future Outlook

5.1 Summary

Double beta decay ($\beta\beta$) is a second order process involving the weak interaction in which an initial nucleus (A, Z) decays to its isobar (A, Z+2) with the emission of two electrons. Two neutrino double beta decay ($2\nu\beta\beta$), which involves emission of two electrons and two anti-neutrinos has been observed experimentally in few isotopes. However, if neutrinos are Majorana particles (with particles and antiparticles being indistinguishable) then the nuclei can undergo a neutrinoless mode of $\beta\beta$ decay, where the final state has only two electrons and no antineutrinos are emitted. Understanding the nature of neutrinos is of fundamental importance to explain the origin of small neutrino masses and possibly to elucidate the matter-antimatter asymmetry observed in nature. After the discovery of neutrino oscillations, there

is a renewed interest in the study of $0\nu\beta\beta$ decay to explore the nature of neutrino. Given the significance of the $0\nu\beta\beta$, there are several ongoing and proposed experiments worldwide employing a variety of novel techniques. Currently the results from calculations of nuclear matrix elements, which are model dependent, introduce a significant uncertainty in the extraction of the effective neutrino mass. Therefore, it is extremely important to measure the $0\nu\beta\beta$ transition rates in different nuclei. In India, a feasibility study to search for $0\nu\beta\beta$ in ^{124}Sn has been initiated using the cryogenic bolometer technique. The TIN.TIN experiment (The INdia-based TIN detector) will be housed at INO, an upcoming underground facility with $\sim$ 1000 m rock cover all around. The ^{124}Sn has a moderate isotopic abundance $\sim$5.8% and a reasonably high Q value of 2292.64 ± 0.39 MeV. Since the constancy of sum energy of two electrons defines the $0\nu\beta\beta$ event, good energy resolution is of paramount importance. Cryogenic bolometers with excellent energy resolution and high sensitivity are well suited for search of $0\nu\beta\beta$. Tin becomes superconducting below 3.7 K and for T$<$100 mK its specific heat has only lattice contributions and can be made into a high resolution, high efficiency bolometric detector.

The R&D related to the fabrication of a large size Tin (superconducting) cryogenic bolometer has been carried out as a part of this thesis work. A custom built cryogen free dilution refrigerator, CFDR-1200, with a high

cooling power of 1.4 mW at 120 mK, has been successfully installed and tested at TIFR, Mumbai. Given the long time scale of $0\nu\beta\beta$ experiment and remote location of underground laboratories, the cryogen free dilution refrigerator is preferred instead of conventional wet system that uses liquid helium supply. Since the sensitivity of $0\nu\beta\beta$ experiment is crucially dependent on the minimization of background radioactivity a bulk shielding is highly desirable inside the cryostat to suppress the background events arising from the materials used for cryostat construction. Therefore, a provision for additional low activity shielding inside the cryostat is also incorporated in the design. The mixing chamber of the CFDR-1200 is capable of supporting and cooling 100 Kg weight and has a cylindrical sample space of 300 mm x 300 mm. The CFDR-1200 is equipped with readout wiring for up to 75 sensors (4 probe measurement). The wiring from room temperature to the 3K stage is done using shielded Phosphor Bronze wire while shielded NbTi wires are used from the 3K to the MC. The superconducting NbTi wires ensure that the thermal heat load on the MC due to large number of wires is negligible. All 300 wires are connected with hermetically sealed connectors at the 50K stage and the 3K stage through two clear shot tubes. This also provides a possibility to mount a preamplifier stage for bolometer pulse processing at 50K, if needed in future. The lowest minimum temperature of 7 mK, measured with the CMN thermometer was achieved without

any external heat load on the system. The temperature calibration of the CMN was verified against a Fixed Point Device. The operating conditions like the flow rate have been optimized for the CFDR-1200. Provisions have been made to minimize mechanical vibrations from the pulsed tube cooler and reduce the radio frequency interference from the surroundings. The setup is being used for the Tin bolometer development and can also be used for other low temperature measurements.

Although Tin micro-calorimeters have shown excellent energy resolution, large size Tin bolometers have not yet been made. It has been reported that the relaxation time constant in superconducting material is longer than expected, which degrades the energy resolution. This can either be due to the long lifetimes of quasi-particles in superconductors or due to anomalous heat capacity at low temperature due to some impurities. It is also quite well known that a small amount of impurity can give rise to high specific heat at these low temperatures. A calorimeter set up has been devised to measure ultra small heat capacity of superconductors below 400 mK in the CFDR-1200. The heat capacity of Tin samples have been investigated to check if anomalous specific heat could affect the energy resolution of an energy calorimeter. The specific heat of Tin has been measured in the temperature rage of 60 - 400 mK and the Debye temperature obtained (199$\pm$9 K) has been found to be consistent with the value reported in literature.

The absence of anomalous heat capacity in the Tin sample at T<100 mK suggests that it should be possible to achieve a complete thermalization of energy in a Tin bolometer absorber. Also, no difference is found between the heat capacity of a polycrystal and a single crystal sample. However, polycrystalline Tin is preferable for the prototype for better thermalization of quasi-particles inside the superconductor compared to single crystals. It should be mentioned that the low temperature thermometry was qualified by measuring the specific heat of Copper, a standard reference material.

Simulations have been carried out to optimize the detector element size for photon background reduction based on hit multiplicity. The possibility to use multiplicity (M) to discriminate between electron ($M = 1$) and gamma rays ($M \geq 1$) has been studied for various detector geometries. The results indicate that the element size of 3x3x3 cm^3 is a preferable choice for the detector element from the calorimetry (to achieve $\Delta T \sim 100\mu$K for E= 2 MeV in 10-20 mK range), granularity (limitation of readout sensors) and gamma ray background reduction capability. The optimal detector module design proposed consists of 27 elements of 3x3x3 cm^3 each, arranged in a cubic array of 3x3x3 such that the central element is covered on all sides by other detector elements. The estimated detection efficiency of this module (mass $\sim$5 Kgs) is $\sim$ 86% for $0\nu\beta\beta$ events. The Tin detector elements can be mounted in a Copper framework (which acts as a thermal bath) with

suitable Teflon supports for mechanical and thermal coupling. The modules can be arranged in a tower geometry for upscaling to large mass detector in a phased manner.

5.2 Future Outlook

A proposal for a laboratory at INO to house a ton scale Tin bolometer detector (TIN.TIN) to investigate $0\nu\beta\beta$ has been made. This experiment is multidisciplinary in nature and the ultra-low event rate involves many challenges like the enrichment of ^{124}Sn, background reduction and readout electronics for low temperature measurements with good resolution.

5.2.1 Schematic of readout electronics for NTD Ge sensors

Sensors and readout electronics are crucial factors as they directly influence the energy resolution. The bolometer readout electronics needs to detect thermal pulses of $\Delta T \sim$10-100μK at base temperature $\sim$10 mK. A typical impedance of the NTD Ge temperature sensor is expected to be $\sim$100 kΩ to 1 MΩ. To obtain a voltage pulse, the thermistor needs a steady bias current $\sim$ 100 pA to 1 nA. The current value has to be kept low to minimize the self-heating of the sensor to the extent possible. The expected pulse height for a 10 μK is $\sim$ 1μV. The fall time of the pulse, which depends

on the capacity of the absorber at base temperature and the thermal link, is estimated to be $\sim$1 to 10 secs (frequency $<$ 15 Hz).

A schematic of the proposed readout electronics is shown in Figure 5.1. At the first stage (pre-amplification), the μV voltage signals can be ampli-

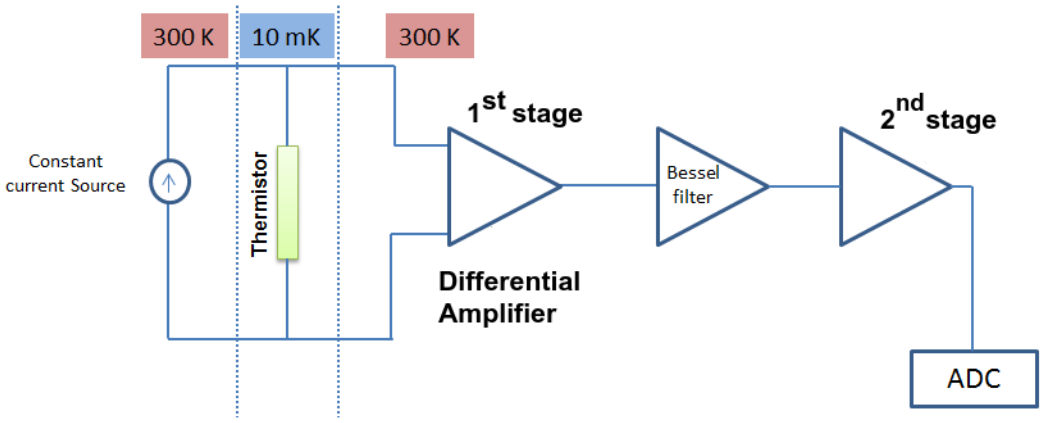

Figure 5.1: A schematic of the proposed readout electronics for the Tin Bolometer.

fied using a low noise differential amplifier to mV scale. A Bessel filter stage, with a unitary gain and a low cut-off frequency ($\sim$15 Hz) is provided to filter the high frequency noise. An additional amplifier (gain $\sim$ 100 -1000) may be necessary to bring the pulse height to $\sim$ 100 mV range prior to digitization of the pulses. It is possible to mount the first differential amplifier stage at 50 K station to reduce the noise. It is expected that a an energy resolution (ΔE) of 0.5% can be obtained in the region of interest.

5.3 Estimated sensitivity of TIN.TIN

The performance of $0\nu\beta\beta$ experiment is usually expressed in terms of sensitivity, defined as the process half life corresponding to the maximum signal hidden by background fluctuation at a given statistical confidence level. At 1σ level one obtains:

$$T_{1/2}^{0\nu}(1\sigma) = \frac{ln2\ N_A\ i\ \varepsilon}{A}\sqrt{\frac{M\ t}{B\ \Delta E}} \tag{5.1}$$

where M is the detector mass, t is the measure time, i is the isotopic abundance of the $\beta\beta$ candidate and ε is the detector efficiency. The ΔE is the energy resolution (σ) at the $Q_{\beta\beta}$ value and B is background rate expressed in units of counts/year/Kg/keV. As mentioned earlier, one of the challenges in the proposed experiment with TIN.TIN detector at INO, is to achieve a background rate of $\sim$0.01 counts/year/Kg/keV, similar to CUORE. For a natural Tin detector, the fraction (i) of ^{124}Sn is 5.8% and as discussed in the last chapter the module efficiency is $\sim$86%. Assuming a ΔE= 10 keV near the $Q_{\beta\beta}$ value and a background rate of 0.01 counts/year/Kg/keV, the sensitivity can be written as

$$T_{1/2}^{0\nu}(1\sigma) = 5.5 \text{ x } 10^{23}\ \sqrt{Mt} \text{ yrs.} \tag{5.2}$$

It is easily seen that even with a counting time of 1 Kg-yr, the estimated sensitivity of the TIN.TIN is four orders of magnitude better than the present existing limits for $0\nu\beta\beta$ decay in ^{124}Sn (2 x 10^{19} yrs [49]). Table 5.1 shows estimated sensitivity for different detector parameters for a measurement time of 1 year.

Table 5.1: Expected $0\nu\beta\beta$ sensitivity of the TIN.TIN for different values of mass, resolution and background level corresponding to a measurement time of 1 year.

Background (counts/year/Kg/keV)	$\Delta E(\sigma)$ (keV)	Mass (Kg)	$T^{0\nu}_{1/2}$ (yrs)
0.1	5	5	5.5 x 10^{23}
0.01	5	5	1.8 x 10^{24}
0.1	5	25	1.2 x 10^{24}
0.01	5	25	3.9 x 10^{24}
0.1	10	25	8.8 x 10^{23}
0.01	10	25	2.8 x 10^{24}
0.01	10	1000	1.8 x 10^{25}

A limit to the effective Majorana neutrino mass can be obtained using the following relation:

$$\frac{1}{T^{0\nu}_{1/2}} = G^{0\nu} \mid M^{0\nu} \mid^2 \frac{\mid m_{ee} \mid^2}{m_e^2} \tag{5.3}$$

Eqn. 5.3 requires a precise knowledge of the phase space factor $G^{0\nu}$ and of the theoretically calculated nuclear matrix elements $M^{0\nu}$ (NME). The value of $G^{0\nu}$ for ^{124}Sn is 9.04 x 10^{-15} yrs, as calculated by Kotila *et. al.* [106].

The calculation of the NME has been carried out using different methods and is shown in Table 5.2. The spread in the theoretical calculations is generally considered as an estimate of the uncertainty.

Table 5.2: Calculated NME ($M^{0\nu}$) for ^{124}Sn according to different nuclear models. (NSM: Nuclear Shell Model, GCM: Generator Coordinate Method, IBM: Interacting Boson Model, PHFB: Projected Hartree-Fock-Bogoliubov)

NSM	GCM	IBM	PHFB
2.62 [107]	4.81 [108]	3.53 [109]	9.76 [110]

From the neutrino oscillation data, in case of inverted mass hierarchy, the effective Majorana neutrino mass $\mid m_{ee} \mid$ is constrained to be between 10 and 100 meV [111, 112]. From the above discussion, it is evident that for a natural Tin detector with a 1 tonne-year observation time, the best expected mass limit will be $\mid m_{ee} \mid$<(0.13 - 1) eV depending upon the $M^{0\nu}$. A significant improvement can be achieved with 90% enrichment, where with a 100 Kg-yr observation time the estimated sensitivity is $\mid m_{ee} \mid \sim$ 20 - 100 meV (PHFB and NSM, respectively), covering almost the entire allowed range for the inverted mass hierarchy of neutrinos. An enriched ^{124}Sn bolometer will also enable the measurement of the half life of $2\nu\beta\beta$ in ^{124}Sn, which is not yet measured.

Glossary A

Glossary

Glossary of terms / acronyms (in order of appearance in the chapters).

$0\nu\beta\beta$: Neutrinoless double beta decay

$2\nu\beta\beta$: Two neutrino double beta decay

CP : Charge Parity

CC : Charged current

NC : Neutral current

LH : Left-handed

RH : Right-handed

SM : Standard Model

PMNS matrix : Pontecorvo-Maki-Nakagawa-Sakata matrix

CPV: Charge parity violation

MSW matter effect: Mikheyev-Smirnov-Wolfenstein matter effect

NS : Normal hierarchy

IS : Inverted hierarchy

INO: India-based Neutrino Observatory

TIN.TIN : The INdia-based TIN detector

NTD Ge : Neutron transmutation doped Germanium

BCS theory : Bardeen, Cooper and Schrieffer's theory

CFDR : Cryogen Free Dilution Refrigerator

Still : The cooling stage in the dilution refrigerator, where the ^{3}He is evaporated and atoms are removed by external pumping.

MC : Mixing chamber

IVC : Inner vacuum chamber

OVC : Outer vacuum chamber

PT- cooler : Pulsed tube cooler

CMN : Cerium Magnesium Nitrate

RF-EMI : Radio frequency and electromagnetic interferences

GI : Galvanized Iron

MS : Mild Steel

FPD : Fixed Point Device

OFHC : Oxygen-free high thermal conductivity

FWHM : Full width at half maximum

NME : Nuclear matrix element

NSM : Nuclear Shell Model

GCM : Generator Coordinate Method

IBM : Interacting Boson Model

PHFB method : Projected Hartree-Fock-Bogoliubov Model

BIBLIOGRAPHY

[1] E. Fermi, Z. Phys. **88** (1934) 161

[2] M. Goeppert Mayer, Phys. Rev. **48** (1935) 512

[3] E. Majorana, Nuovo Cimento **5** (1937) 171

[4] W. Furry, Phys. Rev. **56** (1939) 1184

[5] C. S. Wu, Phys. Rev. **105** (1957) 1413

[6] H. Primakoff and S. P. Rosen, Rep. Prog. Phys. **22** (1959) 121

[7] J. Schechter and J. W. F Valle, Phys. Rev. D **25** (1982) 2951

[8] C. L. Cowan, F. Reines, F. B. Harrison, H. W. Kruse, A. D. McGuire, Science **124** (1956) 103

[9] K. Nakamura and S. T. Petcov, 'Neutrino Masses, Mixing and Oscillations' in J. Beringer et al. (Particle Data Group), Phys. Rev., D **86** (2012) 010001

[10] B. Pontecorvo, Sovietic Physics – Journal of Experimental and Theoretical Physics **6** (1957) 429

[11] B. Pontecorvo, Sovietic Physics – Journal of Experimental and Theoretical Physics, **7** (1958) 172

[12] Z. Maki, M. Nakagawa, and S. Sakata, Progress of Theoretical Physics, **28** (1962) 870.

[13] K. Zuber, 'Neutrino Physics', CRC Press, 2nd ed. (2012) Print.

[14] C. Giunti and C.W. Kim, 'Fundamentals of Neutrino Physics and Astrophysics', Oxford UP (2007) Print

[15] B. Aharmim et al. (SNO collaboration), Phys.Rev. C **88** (2013) 025501

[16] R.Wendell et al. (Super-Kamiokande collaboration), Phys. Rev. D **81** (2010) 092004

[17] A. Gando et al. (KamLAND collaboration), Phys. Rev. D **83** (2011) 052002

[18] P. Adamson et al. (MINOS collaboration), Phys. Rev. Lett. **106** (2011) 181801

[19] M.H. Ahn et al. (K2K collaboration), Phys. Rev. Lett. **90** (2003) 041801

[20] F.P. An et al. (Daya Bay collaboration), Phys. Rev. Lett. **108** (2012) 171803

[21] J.K. Ahn et al. (RENO collaboration), Phys. Rev. Lett. **108** (2012) 191802

[22] Y. Abe et al. (Double Chooz collaboration), Phys. Rev. D **86** (2012) 052008

[23] G.L. Fogli et al., Phys. Rev. D **86** (2012) 013012

[24] M.C. Gonzalez–Garcia et al., JHEP **1212** (2012) 123

[25] S. Bilenky, C Giunti, Mod. Phys. Lett. A **27** (2012) 1230015

[26] V.Tretyak and Y.Zdesenko, Atomic Data and Nuclear Data Tables **80** (2002) 83

[27] I. Ogawa et al., J. Phys. Conf. Ser. **375** (2012) 042018

[28] B. Lehnert, Nucl. Instr. and Meth. A **742** (2014) 254-257

[29] J. F. Wilkerson et al., J. Phys. Conf. Ser. **375** (2012) 042010

[30] A. Barabash, J. Phys. Conf. Ser. **375** (2012) 042012

[31] L. Cardani, J. Phys. Conf. Ser. **375** (2012) 042016

[32] H. Bhang et al., J. Phys. Conf. Ser. **375** (2012) 042023

[33] K. Fushimi et al., J. Phys. Conf. Ser. **203** (2010) 012064

[34] C. Oldorf, J. Phys. Conf. Ser. **375** (2012) 042022

[35] A. S. Barabash, JINST **6** (2011) P08011

[36] P. Gorla, J. Phys. Conf. Ser. **375** (2012) 042013

[37] A. Auger et al., Phys. Rev. Lett. **109** (2012) 032505

[38] A. Gando et al., Phys. Rev. C **85** (2012) 045504

[39] J. Hartnell, J. Phys. Conf. Ser. **375** (2012) 042015

[40] H.V. Klapdor-Kleingrothaus et. al., Phys. Lett. B **586** (2004) 198

[41] F. Feruglio, A. Strumia and F. Vissani, Nucl. Phys. B **637** (2002) 345

[42] C.E. Aalseth et al., Mod. Phys. Lett. A **17** (2002) 1475

[43] M. Agostini et al., Phys. Rev. Let. **111** (2013) 122503

[44] C.Weinheimer and K.Zuber, Ann. Phys. (Berlin) **525** (2013) 565

[45] A. Barabash, arXiv:1403.2870 [nucl-ex]

[46] J.D. Vergados, H. Ejiri and F. Simkovic, Rep. Prog. Phys. **75** (2012) 106301

[47] J. Argyriades et al., Nucl.Phys. A **847** (2010) 168-179

[48] R. Arnold et al., arXiv:1311.5695 [hep-ex]

[49] M.J. Hwang et. al., Astroparticle Physics **31** (2009) 412

[50] E. Andreotte et al., Astropart. Phys. bf 34 (2011) 822

[51] A. Gando et al., Phys. Rev. Lett. **110** (2013) 062502

[52] V. Nanal, EPJ Web of Conferences **66** (2014) 08005

[53] N.K. Mondal, Pramana **79** (2012) 1003

[54] M.K. Bacrania et al., IEEE Trans. on Nucl. Science **56** (2009) 2299

[55] D.A. Bennett et al., Rev. Sci. Instrum. **83** (2012) 093113

[56] D.S. Akerib et. al., Phys. Rev. D **72** (2005) 052009

[57] G. Angloher et. al., The European Physical Journal C **72** (2012) 4

[58] P. Gorla, J. Phys. Conf. Ser., **375** (2012) 042013

[59] C. Arnaboldi et. al., Astropart. Phys., **20** (2003) 91

[60] H.H. Andersen, Nucl. Instr. and Meth. B **15** (1986) 722

[61] Ch. Enss., 'Cryogenic Particle Detection', (Springer, 2005)

[62] E.E. Haller *et. al.,* Infrared Phys. **25** (1985) 257.

[63] K.M. Itoh, Appl. Phys. Lett. **64** (1994) 2121.

[64] P. Gorla et. al., Nucl. Instr. and Meth. A **520** (2004) 641

[65] P. Das, R. de Bruyn Ouboter, K.W. Taconis, Proc. 9th Int. Conf. on Low Temperature Physics, Columbus, OH USA, 1964, Plenum, New York (1965) 1253

[66] D.S. Betts, 'An Introduction to Millikelvin Technology' (Cambridge University Press, 1989)

[67] C. Arnaboldi et. al., Nucl. Instr. and Meth. A **518** (2004) 775

[68] http://www.leidencryogenics.com

[69] http://www.cryomech.com

[70] R.B. Schulz, V.C. Plantz and D.R. Brush, IEEE Transactions on Electromagnetic Compatibility **30** (1988) 187

[71] O.V. Lounasmaa, 'Experimental Principles and Methods below 1K' (Academic, New York, 1974).

[72] F. Pobel, 'Matter and Methods at Low Temperature' (Springer, Berlin, 3rd Ed. 2007).

[73] G. Frossati, J. Low Temp. Phys., **87** (1992) 595

[74] Y. Takano, Rev. Sci. Instrum., **65** (1994) 1667

[75] C. Enss and D. McCammon, J. Low Temp Phys. **151** (2008) 5

[76] L. Cardani, J. Phys.: Conf. Ser. **375** (2012) 042016

[77] J. W. Beeman *et. al.* JINST **8** (2013) P05021

[78] E. Cosulich *et. al.*, Journal Low Temp. Phys. **93** 263 (1993)

[79] E. Perinati, M. Barbara, A. Collura, S. Serio, E. Silver, Nucl. Instrum. Meth. A **531** 459 (2004)

[80] S. B. Kaplan *et al.*, Phys. Rev. B **14** (1976) 4854

[81] P. J. de Visser *et. al.*, Physical Review Letters **106** (2011) 167004

[82] H. Kraus *et. al.* Europhys. Lett. **1** (1986) 161

[83] N.E. Phillips, *C R C Critical Reviews in Solid State Sciences* **2** (1971) Iss. 4,

[84] F. Pobell, Matter and Methods at Low Temperatures, Springer, New York, (1996).

[85] R. Bachmann *et. al.*, Rev. Sci. Instrum. **43** (1972) 205

[86] G. R. Stewart, Rev. Sci. Instrum. **54** (1983) 1

[87] M. Brando, Rev. Sci. Instrum. **80** (2009) 095112

[88] J. P. Shepherd, Rev. Sci. Instrum. **56** (1985) 273

[89] R.E. Schwall, R.E. Howard, and G.R. Stewart, Rev. Sci. Instrum. **4**6 (1975) 1054

[90] H. Tsujii, B. Andraka, K.A. Muttalib, and Y. Takano, Physica B **329-333** (2003) 1522

[91] D. L. Martin, Rev. Sci. Instrum. **38** (1967) 1738

[92] N. Samkharadze, A. Kumar, G.A. Cs'athy, J. Low Temp. Phys. **160** (2010) 246

[93] V. Singh *et. al.*, Pramana - Journal of Physics **81** (2013) 719

[94] S. Riegel and G. Weber, J. Phys. E: Sci. Instrum. **19** (1986) 790

[95] P. Esquinazi, R. König, and F. Pobell, Z. Phys. B - Condensed Matter **87** (1992) 305

[96] J.R. Olson, Cryogenics **33** (1993) 729

[97] H.R.O'Neal and Norman E.Phillips, Phys. Rev. **137** (1965) A748

[98] C.A.Bryant and P.H.Keesom, Phys. Rev. **123** (1961) 491

[99] J.A.Rayne and B.S.Chandrasekhar, Phys. Rev. **120** (1960) 1658

[100] M. Pavan et al., Eur. Phys. J A **36** (2008) 159

[101] www.cern.ch/geant4

[102] R.B. Firestone and V.S. Shirley, Table Of Isotopes, J. Wiley & Sons, 8th Ed (1999)

[103] V.I. Tretyak, private communications.

[104] F. Boehm and P. Vogel, 'Physics of Massive Neutrinos', CUP, 2nd ed. (1992) Print.

[105] J. Suhonen, Nucl. Phys. A **864** (2011) 63

[106] J. Kotila and F. Iachello, Physical Review C **85** (2012) 034316

[107] J. Menendez, A. Poves, E. Caurier and F. Nowacki, Nuclear Physics **818** (2009) 139

[108] T. R. Rodriguez and G. Martinez-Pinedo, Physical Review Letters **105** (2010) 252503

[109] J. Barea and F. Iachello, Physical Review C **79** (2009) 044301

[110] P.K. Rath, private communications.

[111] S. Dell'Oro, S. Marcocci and F. Vissani, Physical Review D **90** (2014) 033005

[112] A. Dueck, W. Rodejohann and K. Zuber, Physical Review D **83** (2011) 113010